International Journal of Precision Engineering and Manufacturing-Green Technology (2023) 10:611–634
https://doi.org/10.1007/s40684-022-00495-z

Online ISSN 2198-0810
Print ISSN 2288-6206

REVIEW

Design and Assessment of Phase-Shifting Algorithms in Optical Interferometer

Sungtae Kim[1] · Jurim Jeon[1] · Yangjin Kim[1] · Naohiko Sugita[2] · Mamoru Mitsuishi[2]

Received: 27 August 2022 / Revised: 27 November 2022 / Accepted: 29 November 2022 / Published online: 13 December 2022
© The Author(s), under exclusive licence to Korean Society for Precision Engineering 2022

Abstract

Silicon wafers and transparent glass plates are major components in the semiconductor industry. In semiconductor devices, the surface shape and optical thickness of the wafers and glass plates are the key parameters for the optimal performance of the devices. Phase-shifting interferometry has been widely used to achieve precision measurements of these parameters. The phase-shifting algorithm significantly affects the interferometric measurement results with phase-shifting interferometry. In this review, we introduce the design and assessment of phase-shifting algorithms in the Fizeau interferometer. Section 2 categorized the phase-shifting algorithms designed by several methods in terms of their error compensation ability. Then, the optical setup of the Fizeau interferometer used for surface and thickness measurement is explained in Sect. 3. In addition, Sect. 4 explained the principle of phase extraction using phase-shifting interferometry and discussed its error sources. Moreover, design methods for the phase-shifting algorithm to eliminate error sources are introduced in Sect. 5. Finally, the error compensation abilities of designed algorithms are estimated by several methods in Sect. 6.

Keywords Fizeau interferometer · Optical thickness · Phase error · Phase-shifting algorithm · Phase-shifting interferometry · Surface shape

1 Introduction

Silicon wafers and transparent glass plates have been widely used in semiconductor industries, such as semiconductor chips and lithography equipment [1–4]. In semiconductor devices, the surface shape and optical thickness of the wafers and glass plates affect the manufacturing process and quality of the devices [5–12]. When the integrated circuits are fabricated using lithography, the fine patterns of the glass plates are projected onto the wafer using a laser. To enhance the reliability of semiconductor devices, the surface shape and optical thickness should be profiled and managed with nanometer measurement accuracy [13–21].

The surface and thickness measurements of wafers and glass plates can be classified into contact and non-contact methods. In the contact method, stylus profilometry is broadly applied to surface and thickness measurements because of its simple operation [22–31]. However, it can cause scratches on the surfaces and it is time-consuming because the stylus tip should be in direct contact with the entire surface of the wafers and glass plates. In contrast, optical interferometry, a non-contact method, is widely applied to precise surface and thickness measurements because of its high resolution and nondestructive and fast measurements [32–38]. Among optical interferometry methods, white-light interferometry is utilized for surface and thickness measurements with nanometer measurement accuracy using the low coherence properties of the light source [39–48]. However, in this method, the measurement accuracy degrades with increasing sample thickness, larger than a few millimeters, owing to the nonlinear translation along the optical axis and refractive-index dispersion.

Phase-shifting interferometry has been broadly applied to surface and thickness measurements to resolve these measurement limitations and achieve nanometer measurement accuracy [49–56]. In phase-shifting interferometry [57–66],

This paper is an invited paper (Invited Review).

✉ Yangjin Kim
yangjin@pusan.ac.kr

[1] School of Mechanical Engineering, Pusan National University, 2 Busandaehak-Ro, Geumjung-Gu, Busan 46241, Republic of Korea

[2] Department of Mechanical Engineering, The University of Tokyo, 7-3-1 Hongo, Bunkyo-Ku, Tokyo 113-8656, Japan

the phase difference between the reference beam and the sample beam is modulated by the phase-shifting technique. The interferograms are acquired at the same intervals of phase-shifting. Then, the phase distribution is calculated using a phase-shifting algorithm [67–76]. Therefore, the phase-shifting algorithm can affect the measurement accuracy of the phase-shifting interferometry.

This review introduces the design methods and assessment of the phase-shifting algorithm for surface and thickness measurements of wafers and glass plates. Section 2 describes the categorization of the phase-shifting algorithms with respect to the error compensation ability of the phase error. Section 3 introduces the optical setup of the Fizeau interferometer using a phase-shifting technique for surface and thickness measurements. Section 4 describes the theory of phase extraction and the error sources in phase-shifting interferometry. The design methods of the phase-shifting algorithm proposed by several authors are explained in Sect. 5. In addition, a performance assessment of the algorithms is introduced. Section 6 presents the evaluation methods for the suppression abilities of the phase-shifting algorithm regarding the phase error. Finally, the conclusions of this study are presented in Sect. 7.

2 Categorization of Phase-Shifting Algorithm

Before explaining the design of the phase-shifting algorithms, we categorize the phase-shifting algorithms. Phase-shifting algorithms can be categorized according to their ability to compensate for error sources, such as harmonics, phase-shift errors, and DC errors, describe in Sect. 4. In this review, phase-shifting algorithms are classified into seven groups. Table 1 shows the categorization of groups according to error compensation ability.

Table 2 shows the categorization of the phase-shifting algorithms designed using several methods described in Sect. 5. In addition, Table 2 shows whether the algorithm satisfies the condition of the visibility maximum described in Sect. 6. Following sections explain the phase-shifting interferometry and design method of the phase-shifting algorithms.

3 Fizeau Interferometer with Phase-Shifting Technique

The Fizeau interferometer with a phase-shifting technique has been widely used for surface and thickness measurements of wafers and glass plates [57, 65]. Because the transmitted and reflected beams in the Fizeau interferometer use the same optical path, this interferometer is resistant to air turbulence. Figure 1a depicts the optical setup of the Fizeau interferometer with the phase-shifting technique, where the diode laser changes the wavelength of the laser beam and modulates the phase of the fringe pattern without mechanical movement of the sample. Generally, the diode laser does not have the preferrable wavelength accuracy and long coherence length because the cavity length changes significantly due to changes in temperature and current flow. However, by setting the front surface of the cavity with an external diffraction grating and mirror (Littman type), the loss of light other than a specific wavelength can be increased. Therefore, by adopting the Littman type diode laser, the coherence length can be larger than 100 mm when the frequency is 1 MHz.

Moreover, the measured sample and target are determined according to the arrangement of the reference surface and sample in the Fizeau interferometer, represented by the green square in Fig. 1a. Figure 1b depicts the three types of optical arrangement of the reference surface and sample in the Fizeau interferometer. The surface and thickness of the transparent glass plate can be measured using the first arrangement by a Fizeau interferometer because the laser beam is transmitted through the glass plate and reflected from the front and rear glass plate surfaces and the reference surface. The second arrangement was applied

Table 1 Categorization of groups according to error compensation ability

Group	Compensation for				
	Harmonics	Linear phase-shift error	Nonlinear phase-shift error	Coupling error	DC error
I	A	N/A	N/A	N/A	N/A
II	A	A	N/A	N/A	N/A
III	A	A	A	N/A	N/A
IV	A	A	N/A	A	N/A
V	A	A	A	A	N/A
VI	A	A	A	N/A	A
VII	A	A	A	A	A

Table 2 Categorization of phase-shifting algorithms

Group	Phase-shifting algorithm	Design method	Visibility maximum	References
I	Synchronous detection	Fourier description	N/A	[77]
	Wyant 4-sample	Trigonometric function	N/A	[78]
	Wyant 3-sample	Trigonometric function	N/A	[79]
II	Schwider and Hariharan 5-sample	Averaging theory	A	[80, 81]
	Larkin-Oreb $N+1$	Fourier description	N/A	[82]
	Zhu 9-sample	Linear equation	A	[83]
III	Schmit and Creath 6-sample	Averaging theory	N/A	[84]
	de Groot 7-sample	Data-sampling window	A	[85]
	Fang 11-sample	Linear equation	A	[72]
IV	Hibino 7-sample	Linear equation	A	[86]
	Surrel 2 $N-1$	Characteristic polynomial	A	[87]
	Hibino 19-sample	Fourier description	N/A	[88, 89]
	Hanayama 2 $N-1$	Characteristic polynomial	A	[90]
	Estrada 9-sample	Fourier description	A	[91]
	Jeon 11-sample	Data-sampling window	A	[92]
V	Hibino 9-sample	Linear equation	N/A	[93]
	Zhang 8-sample	Averaging theory	N/A	[94, 95]
	de Groot 13-sample	Data-sampling window	A	[96]
	Wu 10-sample	Averaging theory	A	[97]
	Shi 13-sample	Data-sampling window	A	[70]
	Kim 3 $N-2$	Characteristic polynomial	A	[98]
	Kumagai 13-sample	Data-sampling window	A	[99]
	Yu 13-sample	Data-sampling window	A	[75]
	Choque 9-sample	Fourier description	A	[100]
	Padilla $C(N-1)-1$	Fourier description	A	[101]
VI	Kim 9-sample	Linear equation	A	[102]
	Choque 8-sample	Fourier description	N/A	[103]
VII	Kim 13-sample	Linear equation	A	[104]
	Bae 19-sample	Linear equation	A	[105]
	Kim 15-sample	Linear equation	A	[106]
	Kim 4 $N-1$	Characteristic polynomial	A	[107]

to surface measurements of the opaque sample. Because the laser beam cannot be transmitted through the opaque sample, the transmitted beam is reflected only from the front sample and reference surfaces. The third arrangement was used for the thickness measurement of the transparent glass plate. Because surface information is not required, the Fizeau interferometer does not contain the reference surface, and the transmitted beam is reflected from the front and rear glass plate surfaces.

Figure 1c depicts the raw interferograms acquired by the Fizeau interferometer with three configurations. The three interferograms correspond to the blank mask, silicon wafer, and optical flat. In addition, Fig. 1d depicts the calculated phase of the surface and thickness of the wafers and glass plates calculated using the interferograms and phase-shifting algorithm. Because of the properties of the phase-shifting algorithm described in Sect. 4, the range of the calculated phase is from $-\pi$ to π, and the calculated phase contains discontinuities. The unwrapping process was used to eliminate discontinuities and obtain the precise surface and thickness of the wafers and glass plates. Figure 1e shows the unwrapped measured results of the surface and thickness of the wafers and glass plates determined by the unwrapping process using the raw phase.

4 Phase Extraction Theory

This section introduces the phase extraction theory of phase-shifting interferometry. In addition, we discuss the error sources occurring in phase-shifting interferometry, which degrade the measurement accuracy.

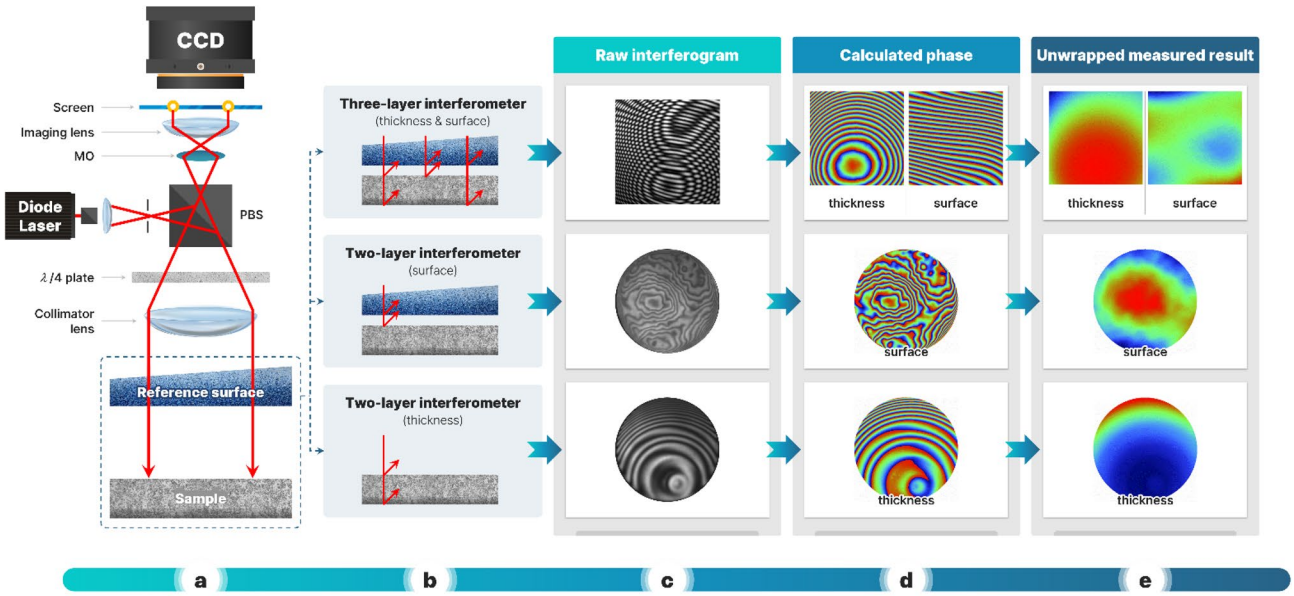

Fig. 1 **a** Optical setup of Fizeau interferometer with phase-shifting technique; **b** three types of optical arrangement of the reference surface and sample in the Fizeau interferometer; **c** raw interferograms of the wafers and glass plates acquired by Fizeau interferometer; **d** calculated phase of the surface and thickness of the wafers and glass plates calculated by interferograms and phase-shifting algorithm; **e** unwrapped measured results of surface and thickness of the wafers and glass plates determined by unwrapping process

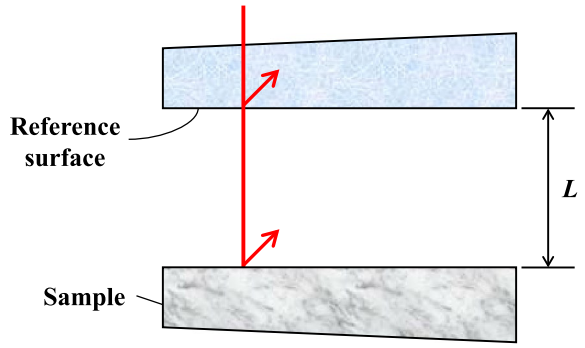

Fig. 2 Simple 2-beam interferometer for measurement of the surface shape of the sample

4.1 Phase-Shifting Interferometry

A simple 2-beam interferometer was considered to conduct the surface measurement. Figure 2 depicts the 2-beam interferometer where L is the air-gap distance between the front sample and reference surfaces.

When measuring the front sample surface using the 2-beam interferometer with the phase-shifting technique, the reflected beams from the front sample and reference surfaces interfere with one another, generating interference fringe patterns. The phase of the fringe pattern corresponds to the phase difference between interfering beams. The intensity of the interferogram is a function of the phase-shift parameter α_r and is given by

$$I_r = S_0 + \sum_{m=1}^{\infty} S_m \cos\left[m\alpha_r + \varphi_m\right] \tag{1}$$

where S_0 is the DC component, and S_m and φ_m are the amplitude and phase of the mth-order harmonics, respectively. Phase φ_1 of the fundamental order corresponding to the surface shape of the sample was the target phase to be calculated.

The M-sample phase-shifting algorithm is used to calculate the target phase and is generally expressed as [77, 108]

$$\varphi^* = \arctan\frac{\sum_{r=1}^{M} H_r I_r}{\sum_{r=1}^{M} G_r I_r} \tag{2}$$

where φ^* is the calculated phase, and G_r and H_r are the sampling weights of the phase-shifting algorithm.

For example, when the reference phase varying from 0 to 2π is separated by equal intervals of $\pi/2$, and only the fundamental order of the harmonics is considered, the intensity of the interferogram is a simple sinusoidal function, as depicted in Fig. 3, and is given as

$$I_r = S_0 + S_1 \cos\left(\alpha_r + \varphi_1\right) \tag{3}$$

where $\alpha_r = 0, \pi/2, \pi, 3\pi/2$ for $r = 1, 2, 3, 4$. Using Eqs. (2) and (3), the target phase is calculated by the trigonometric function and given to

$$\varphi_1 = \arctan\frac{I_2 - I_4}{I_1 - I_3} \tag{4}$$

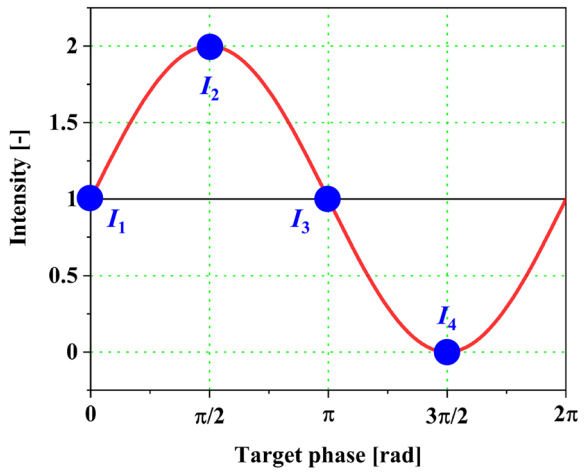

Fig. 3 Intensity of the rth interferogram in the 2-beam interferometer. (under the condition of $S_0 = S_1 = 1$)

where the sampling weights of the above algorithm are given to

$$G_r = [1, 0, -1, 0]$$
$$H_r = [0, 1, 0, -1] \tag{5}$$

This algorithm is the conventional 4-sample phase-shifting algorithm developed by Wyant [78].

4.2 Error Sources of Phase-Shifting Interferometry

In the measurement of the surface shape of the sample using phase-shifting interferometry, the main sources of systematic errors in the calculated phase are harmonics, phase-shift error, and coupling error between the harmonics and phase-shift error [109–116]. The phase-shift parameter α_r, in the phase-shifting technique, should be changed at predetermined intervals. However, the actual phase-shift parameter contains linear miscalibration and nonlinearities because of environmental vibration [117–119], fluctuation of the intensity [120, 121], and nonlinear properties of the piezoelectric transducer (PZT) of the laser diode [122, 123]. The diode laser of New Focus Velocity series has the PZT scanning mode for the interferometric measurement of surface and reported that there is approximately 3% nonlinearity in the PZT behavior [115].

The phase-shift parameter is defined by the ideal phase-shift parameter α_{0r} and phase-shift error ε_q owing to these effects [93]:

$$\alpha_r = \alpha_{0r}\left[1 + \varepsilon_0 + \varepsilon_1\frac{\alpha_{0r}}{\pi} + \varepsilon_2\left(\frac{\alpha_{0r}}{\pi}\right)^2 + \cdots + \varepsilon_p\left(\frac{\alpha_{0r}}{\pi}\right)^p\right] \tag{6}$$

where ε_0 is the linear phase-shift error (linear miscalibration), ε_q is the qth-order nonlinear phase-shift error for $q = 1, 2, \ldots, p$, and $\alpha_{0r} = 2\pi[r - (M+1)/2]/N$, where N is the phase-division number and is an integer.

Substituting Eqs. (1) and (6) into Eq. (2), the phase error $\Delta\varphi$ expanded by the Taylor series is a function of the amplitude of harmonics S_m and the phase-shift error ε_q ($q \geq 0$) [93]:

$$\Delta\varphi = \varphi^* - \varphi_1 = o(S_m) + o(\varepsilon_q) + o(S_m\varepsilon_q) \tag{7}$$

where $m = 2, 3, \ldots, j$; $q = 0, 1, \ldots, p$; and the error terms are as follows:

- $o(S_m)$ is the error from the harmonics. When measuring the surface shape of a highly reflective sample, such as silicon wafers, the effects of the harmonics increase and the observed interferogram consists of combinations of different fringe patterns, which degrades the visibility of the observed interferogram [98, 124].
- $o(\varepsilon_q)$ is the error from the phase-shift error. While calculating the target phase, the linear phase-shift error causes a nonuniform error, and the nonlinear phase-shift error causes both DC and nonuniform errors [93, 102]. The DC error causes critical errors in the measurement of the absolute optical thickness of the sample, and the nonuniform error severely affects the surface measurement [125].
- $o(S_{m\varepsilon q})$ is the error from the coupling error between the harmonics and phase-shift error [93, 126]. For nanometer measurement accuracy, the coupling error should be compensated for by the phase-shifting algorithm.

For example, $o(\varepsilon_1)$ is the first-order nonlinear phase-shift error, and $o(S_2\varepsilon_3)$ is the coupling error between the second-order harmonics and third-order nonlinearity.

A phase-shifting algorithm to compensate for the above phase errors should be used for precise surface and thickness measurements of wafers and glass plates.

5 Design Method of Phase-Shifting Algorithm

This section introduces the design methods of phase-shifting algorithms proposed by several authors to conduct surface and thickness measurements without phase errors. In addition, the performance assessment of the designed algorithms is briefly explained.

5.1 Averaging Theory Between Subsequent Interferograms

Schwider [80, 127] proposed an averaging theory using consecutive interferograms with equal phase-shift intervals to suppress the linear phase-shift error. Schmit and Creath [84] proposed an extended averaging

theory for better insensitivity to linear phase-shift errors.

In averaging theory, the two sets of subsequent *M*-sample interferograms acquired at phase-shift intervals of π/2, where the first set of interferograms overlaps with the second set, are used. Two types of *M*-sample phase-shifting algorithms were derived using the two sets of interferograms. Then, the new $(M+1)$-sample phase-shifting algorithm can be derived by averaging the two types of *M*-sample algorithms.

For the better suppression of the linear phase-shifting error, Schmit and Creath developed a phase-shifting algorithm using the extended averaging theory. Three sets of successive *M*-sample interferograms with equal phase-shift intervals of π/2 were used. Using averaging theory, two types of $(M+1)$-sample algorithms were derived. Then, the averaging theory is reapplied to two types of $(M+1)$-sample algorithms to obtain a new $(M+2)$-sample phase-shifting algorithm.

Schwider developed the 5-sample phase-shifting algorithm by the averaging theory [80, 127], and Creath developed the 5- and 6-sample algorithms using the extended averaging theory [84]. Zhu proposed a 4-sample algorithm using overlapping averaging theory [128]. Zhang developed the 7-, 8-, and 9-sample algorithms using the averaging theory [94, 95], and Wu developed the 10-sample algorithm using the averaging theory [97]. The procedure of the averaging theory is described by Schwider 5-sample algorithm.

When the reference phase changing from 0 to 2π is separated by four equal intervals of π/2, five interferograms are acquired, and the intensity of the interferogram is identical to that in Eq. (3) for $\alpha_r = 0$, π/2, π, 3π/2, and 2π. Using the five interferograms, the target phase was calculated using two types of 4-sample algorithms:

$$\varphi_1 = \arctan\frac{I_2 - I_4}{I_1 - I_3} = \arctan\frac{I_2 - I_4}{I_5 - I_3} \tag{8}$$

By applying the averaging theory to two types of 4-sample algorithms, the Schwider 5-sample algorithm is derived as

$$\varphi_1 = \arctan\frac{2(I_2 - I_4)}{I_1 - 2I_3 + I_5} \tag{9}$$

This 5-sample algorithm was also proposed by Hariharan [81].

For performance assessment of the algorithms, Schwider measured the glass plate surface using the Tyman-Green interferometer [80], Schmit and Creath analyzed the effects of the linear phase-shift error [84], and Zhu carried out a numerical simulation of the phase-shift errors [128]. In addition, Zhang conducted a numerical simulation of the second-order harmonics and phase-shift error and performed 3-D object surface measurements using a fringe projection profilometry system [94, 95]. Wu performed 3-D object surface measurements using a frequency-modulated laser diode interferometric system [97].

5.2 Theory of Fourier Description

Larking and Oreb proposed a design method for a phase-shifting algorithm using the Fourier description of the sampling weight to suppress the phase error [82]. Freischlad and Koliopoulos developed a method for visualizing a phase-shifting algorithm in the frequency domain using the Fourier description of the sampling weights [129].

In the time domain, the sampling functions of the sampling weights are defined as

$$f_1(\alpha) = \sum_{r=1}^{M} H_r \delta(\alpha - \alpha_r) \tag{10}$$

$$f_2(\alpha) = \sum_{r=1}^{M} G_r \delta(\alpha - \alpha_r) \tag{11}$$

where δ(α) is the Dirac delta function.

Using Parseval's equation and Eqs. (10) and (11), the *M*-sample phase-shifting algorithm in Eq. (2) can be expressed as

$$\varphi^* = \arctan\frac{\sum_{r=1}^{M} H_r I_r}{\sum_{r=1}^{M} G_r I_r} = \arctan\frac{\int_{-\infty}^{\infty} F_1(\nu) J(\nu) d\nu}{\int_{-\infty}^{\infty} F_2(\nu) J(\nu) d\nu} \tag{12}$$

where ν is the frequency variable, and $F_1(\nu)$, $F_2(\nu)$, and $J(\nu)$ are the Fourier transforms of $f_1(\alpha)$, $f_2(\alpha)$, and $I(\alpha)$, respectively. Because the sampling weights and phase-shift parameters have the symmetric properties of $G_r = G_{M+1-r}$, $H_r = -H_{M+1-r}$, and $\alpha_r = -\alpha_{M+1-r}$ [98], the sampling functions in the frequency domains $F_1(\nu)$ and $F_2(\nu)$ become imaginary and real functions, respectively.

$$F_1(\nu) = \sum_{r=1}^{M} H_r \exp\left(-i\alpha_r \nu\right) = -i \sum_{r=1}^{M} H_r \sin\left(\alpha_r \nu\right) \tag{13}$$

$$F_2(\nu) = \sum_{r=1}^{M} G_r \exp\left(-i\alpha_r \nu\right) = \sum_{r=1}^{M} G_r \cos\left(\alpha_r \nu\right) \tag{14}$$

where *i* is the imaginary unit.

For the design of the phase-shifting algorithm to calculate the target phase with the suppression of the phase error, Eqs. (13) and (14) should satisfy the following conditions.

– To calculate the exact phase of the fundamental frequency, the amplitudes of Eqs. (13) and (14) are identical at the fundamental frequencies [82]:

$$iF_1(\nu) = F_2(\nu),\ (\nu = 1) \tag{15}$$

–To suppress the effects of the jth-order harmonics, the amplitudes of Eqs. (13) and (14) at harmonic frequencies of $\nu = 2, 3, \ldots, j$ are zero [86]:

$$F_1(\nu) = F_2(\nu) = 0,\ (\nu = 2, 3, \ldots, j) \tag{16}$$

– To eliminate the linear and pth-order nonlinear phase-shift errors, the $(q+1)$ th-order derivatives of Eqs. (13) and (14) at a fundamental frequency of zero [82, 93]:

$$\left.\frac{d^{(q+1)}iF_1(\nu)}{d\nu^{(q+1)}}\right|_{\nu=1} = \left.\frac{d^{(q+1)}F_2(\nu)}{d\nu^{(q+1)}}\right|_{\nu=1},\ (q = 0, 1, \ldots, p) \tag{17}$$

– To compensate for the coupling error between the harmonics and phase-shift error, the $(q+1)$ th-order derivatives of Eqs. (13) and (14) at harmonic frequencies of $\nu = 2, 3, \ldots, j$ are zero [93]:

$$\left.\frac{d^{(q+1)}iF_1(\nu)}{d\nu^{(q+1)}}\right|_{\nu=2,3,\ldots,j} = \left.\frac{d^{(q+1)}F_2(\nu)}{d\nu^{(q+1)}}\right|_{\nu=2,3,\ldots,j} = 0,\ (q = 0, 1, \ldots, p) \tag{18}$$

Using the theory of Fourier description, Larkin and Oreb developed the $N+1$ algorithm [82], and Hibino proposed two types of 19-sample algorithms [88, 89]. Additionally, by applying the frequency transfer function to the sampling weights of the algorithm [130, 131], Estrada developed a 9-sample algorithm [91], Choque developed a 9-sample algorithm [100], and Padilla developed the $C(N-1)-1$ algorithm (where C is the power of the frequency transfer function) [101]. The procedures for deriving the phase-shifting algorithm using the Fourier description are described by the $N+1$ algorithm and the 19-sample algorithm.

In the case of the $N+1$ algorithm ($N=6$), which can eliminate the fourth-order harmonics and linear phase-shift error, the sampling weights of the $N+1$ algorithm can be derived using Eqs. (15)–(17). The target phase is calculated using the $N+1$ algorithm and is defined as

$$\varphi_1 = \arctan\frac{-I_1 + 3I_2 + 3I_3 - 3I_5 - 3I_6 + I_7}{\sqrt{3}\left(-I_1 - I_2 + I_2 + 2I_4 + I_5 - I_6 - I_7\right)} \tag{19}$$

Hibino developed a 19-sample algorithm to compensate for the effects of the 10th-order harmonics and phase-shift error caused by refractive-index dispersion [88]. Using Eqs. (15)–(18), the sampling weights of the 19-sample algorithm can be derived as

$$\begin{aligned}\left[G_r\right]_{M=19} &= \left[-1, 1-2\sqrt{3}, -5, -4\sqrt{3}, -7, -1-2\sqrt{3}, 1, 4\sqrt{3}, 12, 8\sqrt{3}\right]\\ \left[H_r\right]_{M=19} &= \left[\sqrt{3}-1, 1, 1, -2, 1-4\sqrt{3}, -11, -1-7\sqrt{3}, -12, -4\sqrt{3}, 0\right]\end{aligned} \tag{20}$$

where the rest of the sampling weights in Eq. (20) can be determined from the symmetric properties of $G_r = G_{20-r}$ and $H_r = -H_{20-r}$.

To understand and evaluate the behaviors of the phase-shifting algorithm, the algorithm is visualized in the frequency domain using Eqs. (13) and (14) [129]. Figure 4 represents Eqs. (13) and (14) of the $N+1$ algorithm [82] and the 19-sample algorithm [88], respectively.

From Fig. 4a, the amplitudes and first-order derivatives of Eqs. (13) and (14) match at the fundamental frequency, and the amplitudes at the harmonic frequencies of $m=2$, 3, and 4 are zero. Therefore, the $N+1$ algorithm can suppress the fourth-order harmonics and linear phase-shift error.

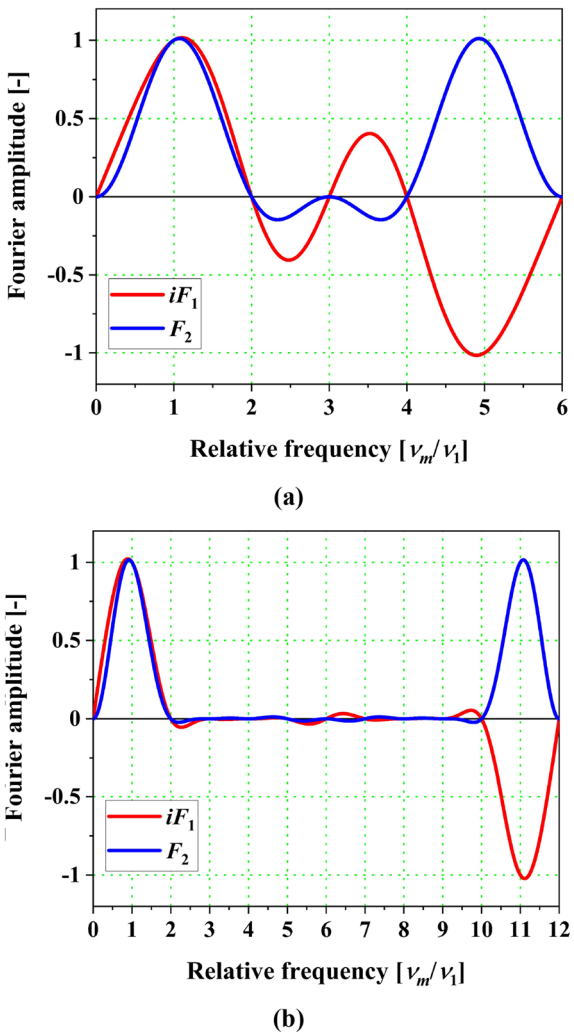

Fig. 4 Sampling functions iF_1 and F_2 of **a** Larkin and Oreb $N+1$ algorithm for $N=6$ [82] and **b** Hibino 19-sample algorithm [88]

From Fig. 4b, the amplitudes and first-order derivatives of Eqs. (13) and (14) are identical at the fundamental frequencies. Moreover, the amplitudes at the harmonic frequencies of $m=2, 3, \ldots, 10$ are zero, and that of the sidelobes between the harmonic frequencies is minimized. Thus, the 19-sample algorithm can suppress the 10th-order harmonics, linear phase-shift error, and refractive-index dispersion.

For performance assessment of the algorithms, Larkin and Oreb visualized the algorithms using the sampling functions of the sampling weights [82], and Hibino measured the surface shape of BK7 using a Fizeau interferometer [88]. Furthermore, Choque measured the surface shape of a thin aluminum film using a Michelson interference microscope [100], and Padilla performed a numerical simulation under various experimental conditions [101].

5.3 Theory of Linear Equations

Hibino proposed linear equations to derive an error resistance phase-shifting algorithm [86, 93, 132–134]. The linear equations comprising the sampling weights are the conditions for compensating for the phase error.

The phase error in Eq. (7) is rewritten as

$$\Delta\varphi = \arctan\frac{\sin\varphi_1 - \pi\sum_{r=1}^{M}\sum_{q=0}^{p}\varepsilon_q\left(\frac{\alpha_{0r}}{\pi}\right)^{q+1}H_r\sin\left(\alpha_{0r}-\varphi_1\right)}{\cos\varphi_1 - \pi\sum_{r=1}^{M}\sum_{q=0}^{p}\varepsilon_q\left(\frac{\alpha_{0r}}{\pi}\right)^{q+1}G_r\sin\left(\alpha_{0r}-\varphi_1\right)} - \varphi_1 \tag{21}$$

To simplify the phase error, the symmetric properties of sampling weights and the phase-shift parameter [93] and the linear equations for suppressing the jth-order harmonics defined by following Eqs. (22) and (23) are used [86]:

$$\sum_{r=1}^{M} G_r\sin\left(m\alpha_{0r}\right) = \sum_{r=1}^{M} H_r\cos\left(m\alpha_{0r}\right) = 0 \tag{22}$$

$$\sum_{r=1}^{M} G_r\cos\left(m\alpha_{0r}\right) = \sum_{r=1}^{M} H_r\sin\left(m\alpha_{0r}\right) = \delta(m,1) \tag{23}$$

where $m=0, 1, 2, \ldots, j$ and δ is the Kronecker delta function in the above equation. Using the approximation $[(1+\omega)\tan\varphi]\sim\varphi+(\omega/2)\sin2\varphi$, and Eqs. (22) and (23), the phase error is defined as [93]

$$\begin{aligned}\Delta\varphi = {} & \frac{1}{2}\sum_{q=0}^{p}\varepsilon_q\left[\frac{\Theta_q(\varphi_1)}{\cos\varphi_1} - \frac{\Omega_q(\varphi_1)}{\sin\varphi_1}\right]\sin\left(2\varphi_1\right) \\ & + \frac{1}{2}\sum_{q=0}^{p}\sum_{m=2}^{j}\varepsilon_q\frac{S_m}{S_1}\left[\frac{\Xi_{m,q}(\varphi_1)}{\cos\varphi_1} - \frac{\Psi_{m,q}(\varphi_1)}{\sin\varphi_1}\right]\sin\left(2\varphi_1\right)\end{aligned} \tag{24}$$

where the error coefficients in Eq. (24) are expressed as

$$\Theta_q(\varphi_1) = \pi\sum_{r=1}^{M} G_r\left(\frac{\alpha_{0r}}{\pi}\right)^{q+1}\sin\left(\alpha_{0r}-\varphi_1\right) \tag{25}$$

$$\Omega_q(\varphi_1) = \pi\sum_{r=1}^{M} H_r\left(\frac{\alpha_{0r}}{\pi}\right)^{q+1}\sin\left(\alpha_{0r}-\varphi_1\right) \tag{26}$$

$$\Xi_{m,q}(\varphi_1) = \pi m\sum_{r=1}^{M} G_r\left(\frac{\alpha_{0r}}{\pi}\right)^{q+1}\sin\left(m\alpha_{0r}-\varphi_m\right) \tag{27}$$

$$\Psi_{m,q}(\varphi_1) = \pi m\sum_{r=1}^{M} H_r\left(\frac{\alpha_{0r}}{\pi}\right)^{q+1}\sin\left(m\alpha_{0r}-\varphi_m\right) \tag{28}$$

In Eqs. (25)–(28), the error coefficients Θ_q and Ω_q are related to the phase-shift error, and $\Xi_{m,q}$ and $\Psi_{m,q}$ are associated with the coupling error between the harmonics and phase-shift error.

Using Eqs. (25) and (26), the first term on the right side of Eq. (24) is given by:

$$\begin{aligned}\sum_{q=0}^{p}\varepsilon_q\left[\frac{\Theta_q(\varphi_1)}{\cos\varphi_1} - \frac{\Omega_q(\varphi_1)}{\sin\varphi_1}\right]\sin\left(2\varphi_1\right) \\ = \frac{\pi}{2}\sum_{q=0}^{p}\varepsilon_q\left(X_q\sin2\varphi_1 + Y_q + Z_q\cos2\varphi_1\right)\end{aligned} \tag{29}$$

where the error coefficients X_q, Y_q, and Z_q are expressed as

$$X_q = \frac{1}{2}\sum_{r=1}^{M}\left(\frac{\alpha_{0r}}{\pi}\right)^{q+1}\left(G_r\sin\alpha_{0r} + H_r\cos\alpha_{0r}\right) \tag{30}$$

$$Y_q = -\frac{1}{2}\sum_{r=1}^{M}\left(\frac{\alpha_{0r}}{\pi}\right)^{q+1}\left(G_r\cos\alpha_{0r} + H_r\sin\alpha_{0r}\right) \tag{31}$$

$$Z_q = \frac{1}{2}\sum_{r=1}^{M}\left(\frac{\alpha_{0r}}{\pi}\right)^{q+1}\left(G_r\sin\alpha_{0r} - H_r\cos\alpha_{0r}\right) \tag{32}$$

Because the sampling weights and phase-shift parameters have symmetric properties, X_q becomes zero when q is an even value, and Y_q and Z_q become zero when q is zero and odd values [135].

In Eq. (29), coefficient Y_q is the DC error because this coefficient is not related to the target phase. In contrast, the coefficients X_q and Z_q are nonuniform errors because these error terms are multiplied by the target phase. The sampling weights of the algorithm should satisfy the following linear equations to suppress the DC and nonuniform errors caused by the phase-shift error:

$$\sum_{r=1}^{M} \alpha_{0r}^{q+1}\left(G_r \sin\alpha_{0r} + H_r \cos\alpha_{0r}\right) = 0 \tag{33}$$

$$\sum_{r=1}^{M} \alpha_{0r}^{q+1}\left(G_r \cos\alpha_{0r} + H_r \sin\alpha_{0r}\right) = 0 \tag{34}$$

$$\sum_{r=1}^{M} \alpha_{0r}^{q+1}\left(G_r \sin\alpha_{0r} - H_r \cos\alpha_{0r}\right) = 0 \tag{35}$$

where $q=0, 1, 2, \ldots, p$.

Furthermore, the second term on the right side of Eq. (24) should be zero to suppress the coupling error between the harmonics and phase-shift error:

$$\sum_{q=0}^{p}\sum_{m=2}^{j} \varepsilon_q \frac{S_m}{S_1}\left[\frac{\Xi_{m,q}(\varphi_1)}{\cos\varphi_1} - \frac{\Psi_{m,q}(\varphi_1)}{\sin\varphi_1}\right]\sin\left(2\varphi_1\right) = 0 \tag{36}$$

By substituting Eqs. (27) and (28) into Eq. (36), the linear equations for suppressing the coupling error are derived as follows:

$$\sum_{r=1}^{M} \alpha_{0r}^{q+1} G_r \sin m\alpha_{0r} = 0 \tag{37}$$

$$\sum_{r=1}^{M} \alpha_{0r}^{q+1} H_r \sin m\alpha_{0r} = 0 \tag{38}$$

$$\sum_{r=1}^{M} \alpha_{0r}^{q+1} G_r \cos m\alpha_{0r} = 0 \tag{39}$$

$$\sum_{r=1}^{M} \alpha_{0r}^{q+1} H_r \cos m\alpha_{0r} = 0 \tag{40}$$

where $m=0, 1, 2, \ldots, j$ and $q=0, 1, 2, \ldots, p$.

Through the linear equations of the sampling weights, Hibino developed the 7-, 9-, and 11-sample algorithms [86, 93], and Sun developed a 36-sample algorithm with a window function [74]. To suppress the DC error, Kim developed the 9- [102] and 13-sample algorithm [104], Bae developed the two types of 19-sample algorithms [105] and 11-sample algorithms [136], and Kim developed the 15-sample algorithm [106]. Moreover, Choque proposed a frequency transfer function of the phase-shifting algorithm to suppress DC error [103].

In addition to the linear equations proposed by Hibino, Fang and Zhu derived linear equations for suppressing the phase-shift error caused by the 0th-order effect [72, 83]. Fang developed the 11-sample algorithm [72], and Zhu developed the 9-sample algorithm [83].

The procedures for deriving the phase-shifting algorithm using linear equations are explained by the Hibino 7-sample algorithm and the Kim 9-sample algorithm. To derive the 7-sample algorithm that can suppress the second-order harmonics, linear phase-shift error, and coupling error, the sampling weights of the algorithm and the phase-shift parameter are set as

$$\begin{aligned} G_r &= \left[G_1, G_2, G_3, G_4, G_3, G_2, G_1\right] \\ H_r &= \left[H_1, H_2, H_3, H_4, -H_3, -H_2, -H_1\right] \end{aligned} \tag{41}$$

$$\alpha_{0r} = \frac{\pi}{2}(r-4) \tag{42}$$

Using Eqs. (41) and (42) and linear equations, the sampling weights of the 7-sample algorithm can be obtained, and the target phase is calculated by

$$\varphi_1 = \arctan\frac{I_1 - 3I_3 + 3I_5 - I_7}{2\left(-I_2 + 2I_4 - I_6\right)} \tag{43}$$

In the case of the Kim 9-sample algorithm, the sampling weights composed of the discrete Fourier transform (DFT) term and the window function w_r are applied to the linear equations [137] and are given by

$$G_r = w_r \cos\alpha_{0r} \tag{44}$$

$$H_r = w_r \sin\alpha_{0r} \tag{45}$$

To suppress the second-order harmonics and DC error caused by the first-order nonlinear phase-shift error, the window function, and phase-shift parameter were set as

$$w_r = \left[w_1, w_2, w_3, w_4, w_5, w_4 w_3, w_2, w_1\right] \tag{46}$$

$$\alpha_{0r} = \frac{\pi}{2}(r-5) \tag{47}$$

Solving the linear equations using Eqs. (45)–(48), the sampling weights of the 9-sample algorithm can be derived, and the target phase can be calculated as follows:

$$\varphi_1 = \arctan\frac{I_2 + 9I_4 - 9I_6 - I_8}{I_1 + 4I_3 - 10I_5 + 4I_7 + +I_9} \tag{48}$$

To evaluate the abilities of Hibino 7-sample algorithm [86] and Kim 9-sample algorithm [102], two algorithms are visualized in the frequency domain using Eqs. (13) and (14) explained in Sect. 5.2.

From Fig. 5a, amplitudes and gradients of Eqs. (13) and (14) at the fundamental frequency are same, indicating that the 7-sample algorithm can calculate the target phase

while suppressing the linear phase-shift error. Moreover, the amplitudes and the first-order derivatives of Eqs. (13) and (14) are zero at the frequency of the second-order harmonics, which means that this algorithm can compensate for the coupling error caused by the second-order harmonics and linear phase-shift error.

Figure 5b shows that the amplitudes and the second-order derivatives of Eqs. (13) and (14) are identical at the fundamental frequency, which means that this algorithm can suppress the linear and the first-order nonlinear phase-shift errors. The amplitudes of Eqs. (13) and (14) at the frequency of the second-order harmonics are zero, indicating that the 9-sample algorithm can eliminate the second-order harmonics. In addition, the configuration of Eqs. (13) and (14) at the fundamental frequency is flat, which means that DC error caused by the first-order nonlinear phase-shift error can be compensated by the 9-sample algorithm [102].

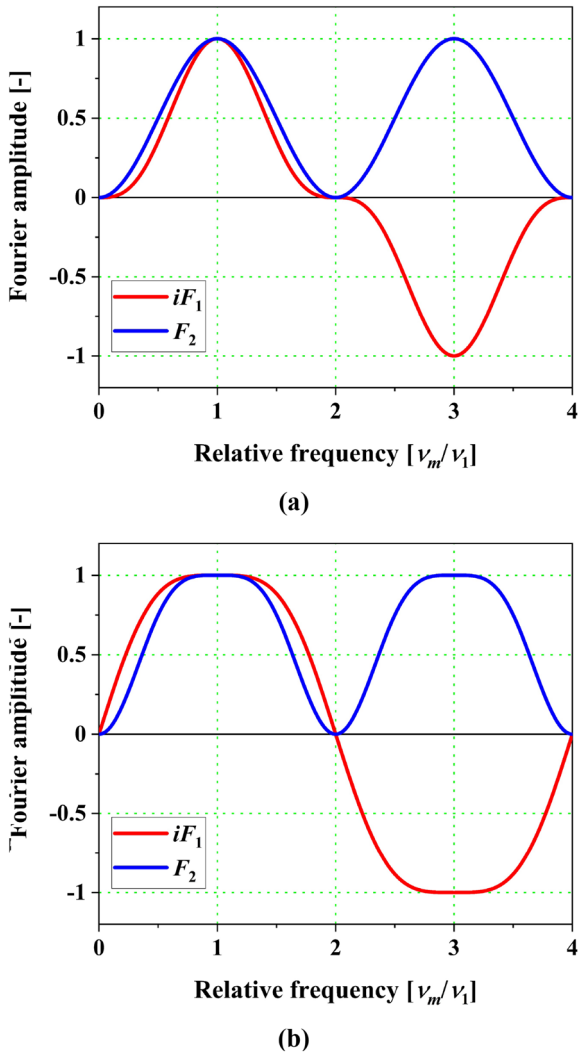

Fig. 5 Sampling functions iF_1 and F_2 of **a** Hibino 7-sample algorithm and [86] **b** Kim 9-sample algorithm [102]

To assess the performance of the algorithms, Hibino analyzed the phase error and visualized the algorithms using the sampling functions of the sampling weights [86, 93], and Sun measured the glass plate surface shape and optical thickness using the Fizeau interferometer. In addition, Kim tested the optical thickness of the fused silica plate [102] and glass plate [104] using the Fizeau interferometer; Bae measured the optical thickness of the glass plate [105] and BK7 [136] using the Fizeau interferometer; Kim measured the glass plate optical thickness using the Fizeau interferometer [106], and Choque performed a numerical simulation of the DC error [103]. Fang carried out a numerical simulation of the lateral shearing interference [72], and Zhu tested a glass plate using a lateral shearing interferometer [83].

5.4 Theory of Data-Sampling Window

De Groot proposed a method for designing a phase-shifting algorithm that can manage the phase error using a data-sampling window [85, 96]. de Groot explained the conditions for suppressing the phase error using the Fourier transforms of the data-sampling window and derived the sampling weights using the data-sampling window.

The Fourier transform of the intensity defined in Eq. (3) is used to calculate the target phase with a data-sampling window as follows:

$$\begin{aligned} J(\nu) &= \sum_{r=1}^{M} I(\alpha_{0r}) w_r \exp\left(-i\alpha_{0r}\nu\right) \\ &= \sum_{r=1}^{M} \left\{ S_0 W(\nu) + 0.5 S_1 \begin{bmatrix} W(\nu-\nu_1)\exp\left(i\varphi_1\right) \\ +W(\nu+\nu_1)\exp\left(-i\varphi_1\right) \end{bmatrix} \right\} \end{aligned} \tag{49}$$

where $W(\nu)$ is the Fourier transform of the data-sampling window and is defined as

$$W(\nu) = \sum_{r=1}^{M} w_r \exp\left(-i\alpha_{0r}\nu\right) \tag{50}$$

To calculate the target phase at fundamental frequency ν_1, the Fourier transform of the data-sampling window should satisfy the following conditions [85]:

$$W(\nu_1) = W(2\nu_1) = 0 \tag{51}$$

Using the above conditions, the target phase is calculated as

$$\varphi_1 = \frac{\mathrm{Im}\left[J(\nu_1)\right]}{\mathrm{Re}\left[J(\nu_1)\right]} \tag{52}$$

Moreover, the Fourier transform of the data-sampling window has minimal sidelobes between harmonic frequencies to suppress the phase-shift error [85].

Using the data-sampling window with suppression of the phase error, the sampling weights of the phase-shifting algorithm can be derived as follows [85]:

$$\begin{aligned} G_r &= \text{round}\left(Kw_r \cos\alpha_{0r}\right) \\ H_r &= \text{round}\left(Kw_r \sin\alpha_{0r}\right) \end{aligned} \tag{53}$$

where K is an approximation parameter and an integer.

Several authors have developed phase-shifting algorithms using data sampling windows. de Groot proposed a 7-sample algorithm [85] and a 13-sample algorithm [96], Shi developed a 13-sample algorithm using the self-convolution of the rectangular window [70], Kumagai developed the 13-sample algorithm using the averaged three-triangle window [99], Yu developed the 13-sample algorithm using the least-squares method [75], and Jeon developed the 11-sample algorithm [92]. The process of deriving the phase-shifting algorithm using the data-sampling window is described by the de Groot 7-sample and Jeon 11-sample algorithms.

de Groot derived the 7-sample algorithm with the von-Hann window that is defined as

$$w_r = 0.5 + 0.5\cos\left[\frac{2\pi}{N_w}\left(r - \frac{M+1}{2}\right)\right] \tag{54}$$

where N_w is a periodic parameter for the data sampling window. Figure 6 shows the von-Hann window satisfies the conditions defined in Eq. (53) and has small sidelobes when $N=4$, $N_w=8$, and $M=7$. The parameters were adjusted to derive the 7-sample algorithm as $N=4$, $N_w=8$, and $K=8$. Then, the target phase can be calculated as follows:

$$\varphi_1 = \arctan\frac{I_1 - 7I_3 + 7I_5 - I_7}{-4I_2 + 8I_4 - 4I_4} \tag{55}$$

Similarly, Jeon developed an 11-sample algorithm using the Blackman window. The Blackman window is defined as:

$$w_r = 0.42 - 0.5\cos\left(\frac{2\pi}{N_w}r\right) + 0.8\cos\left(\frac{4\pi}{N_w}r\right) \tag{56}$$

In Fig. 6, the Fourier transform of the Blackman window when $N=4$, $N_w=12$, and $M=11$ satisfies Eq. (53) and has fewer sidelobes than the von Hann window. Using the parameters $M=11$, $N=4$, $N_w=12$, and $K=28$, the 11-sample algorithm can be derived, and the target phase is calculated as

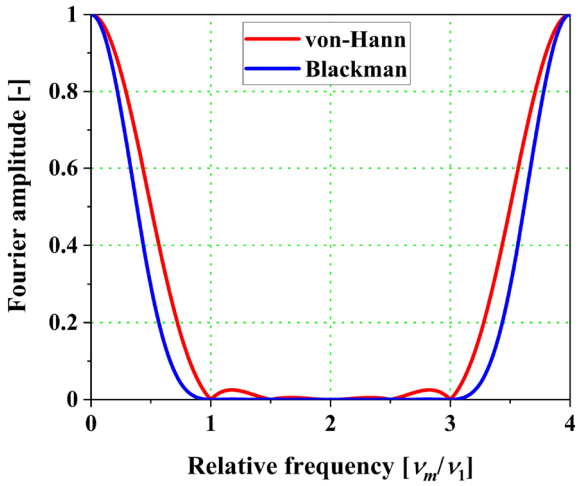

Fig. 6 Fourie transforms of the von-Hann and Blackman windows

$$\varphi_1 = \arctan\frac{-I_1 + 10I_3 - 25I_5 + 25I_7 - 10I_3 + I_{11}}{4I_2 - 18I_4 + 28I_6 - I_8 + 4I_{10}} \tag{57}$$

The algorithms were visualized in the frequency domain using Eqs. (13) and (14), as discussed in Sect. 5.2, to estimate the phase-shifting algorithm derived from the data-sampling window. Figure 7 shows Eqs. (13) and (14) for the de Groot 7-sample [85] and Jeon 11-sample algorithms [92], respectively.

From Fig. 7a, the amplitudes and fourth-order derivatives of Eqs. (13) and (14) at the fundamental frequency are identical, implying that this algorithm can compensate for the second-order nonlinear phase-shift error in the calculated phase. In addition, the amplitudes of Eqs. (13) and (14) at the second-order harmonic frequency are zero, indicating that the 7-sample algorithm can suppress the second-order harmonics.

From Fig. 7b, because the sampling functions have the same amplitude and first-order derivatives at the fundamental frequency, the 11-sample algorithm can compensate for the linear phase-shift error. Moreover, the amplitudes and first derivatives of Eqs. (13) and (14) at the second-order harmonic frequency are zero, implying that this algorithm can eliminate the second-order harmonics and coupling error between the second-order harmonics and the linear phase-shift error.

For performance assessment of the algorithms, de Groot estimated the phase error caused by the phase-shift error and measured the glass plate surface using a Fizeau interferometer [85, 96]. Shi conducted a numerical simulation regarding the phase-shift error [70], and Kumagai tested the spherical surface using a Fizeau interferometer [99]. Furthermore, Yu conducted a numerical simulation of the phase-shift error [75], and Jeon measured the silicon wafer surface using a Fizeau interferometer [92].

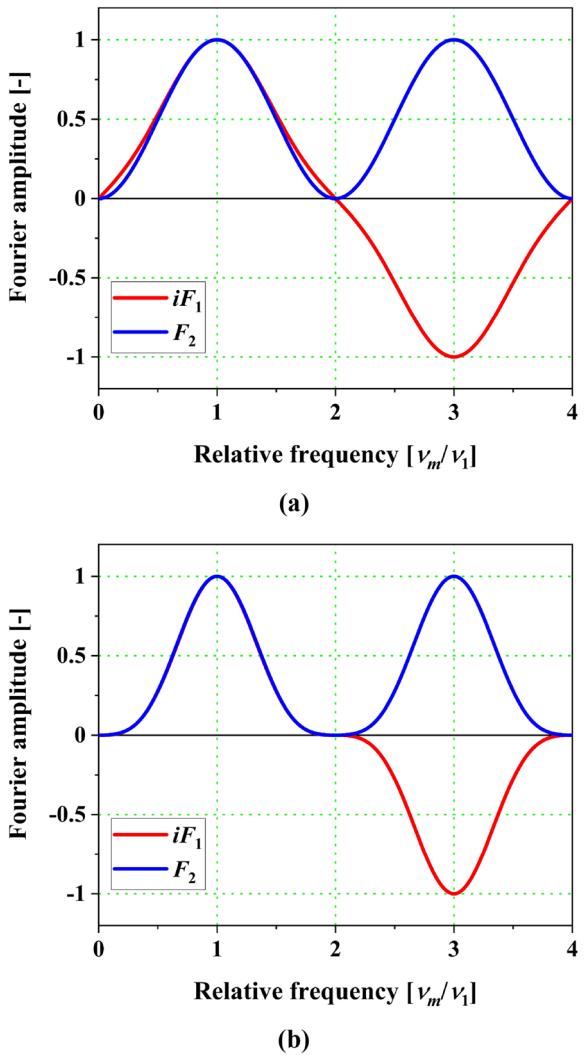

Fig. 7 Sampling functions iF_1 and F_2 of **a** de Groot 7-sample algorithm and [85] **b** Jeon 11-sample algorithm [92]

5.5 Theory of Characteristic Polynomial

Surrel proposed a design method for a phase-shifting algorithm based on a characteristic polynomial [87]. In this method, the root position of the characteristic polynomial corresponds to the algorithm properties. The characteristic polynomial of the M-sample phase-shifting algorithm is given as follows [87]:

$$P(x) = \sum_{r=1}^{M} \left(G_r - iH_r\right)x^{r-1} \tag{58}$$

where $x = \exp(2\ m\pi i/N)$. The resistance of the algorithm to the phase error can be determined by the powers and locations of the roots of the characteristic polynomial.

Moreover, the characteristic diagram visualizes the roots of the characteristic polynomial in a complex plane. The characteristic diagram is a unit circle on the complex plane divided by an equal angle of $2\pi/N$ rad, where each divided point corresponds to harmonics. Therefore, the characteristic polynomial of the algorithm can be expressed by factorization consisting of harmonics:

$$P(x) \propto \prod_{\substack{m=-1 \\ m\neq 1}}^{j} (x - \zeta^m)^k \tag{59}$$

where k is the multiplicity of the roots, and ζ corresponds to the fundamental order of the harmonics on the characteristic diagram, defined as $\zeta = \exp(2\pi i/N)$.

The characteristic polynomial of the algorithm should satisfy the following root positioning conditions to compensate for the phase error [82, 87, 138]:

- To suppress the jth-order harmonics, N is adjusted to $j+2$ [86], and the single roots should be positioned on the divided point of the characteristic diagram, except at $m=1$ [87]. In other words, the factorization of the characteristic polynomial should have $[x - \exp(\exp(2\ m\pi i/N)]$ for $m = 0, \pm 2, \pm 3, \ldots, \pm j$.
- To eliminate the linear and qth-order nonlinear phase-shift errors in the calculated phase, $(q+2)$ multiple roots should be positioned at $m=+1$ on the characteristic diagram, implying that the factorization of the characteristic polynomial should have $[x - \exp(\exp(-2\pi i/N)]^{(q+2)}$ for $q = 0, 1, 2, \ldots, p$.
- To suppress the coupling error between the jth-order harmonics and the linear and qth-order nonlinear phase-shift errors, $(q+2)$ multiple roots should be positioned at $m = 0, \pm 2, \pm 3, \ldots, \pm j$ on the characteristic diagram, indicating that the factorization of the characteristic polynomial should consist of $[x$—$\exp(\exp(2\ m\pi i/N)]^{(q+2)}$ for $m = 0, \pm 2, \pm 3, \ldots, \pm j$ and $q = 0, 1, 2, \ldots, p$.

Moreover, a conventional phase-shifting algorithm can be estimated using a characteristic diagram. Using Eqs. (9) and (58), the characteristic diagram of the Schwider and Hariharan 5-sample algorithm is shown in Fig. 8. As shown in Fig. 8, the single roots are positioned at $m = 0, 2$, and the double root is positioned at $m = -1$ on the characteristic diagram. Based on the root positioning conditions of the characteristic polynomial, the 5-sample algorithm can suppress the second-order harmonics and linear phase-shift error.

Several authors have developed phase-shifting algorithms using the characteristic polynomial. Surrel proposed the $2N-1$ algorithm [87], and Hanayama developed a modified $2N-1$ algorithm [90]. Kim developed the $3N-2$ [98], $4N-3$ [139], $5N-4$ [140], $6N-5$ [141], $7N-6$ [142] algorithms

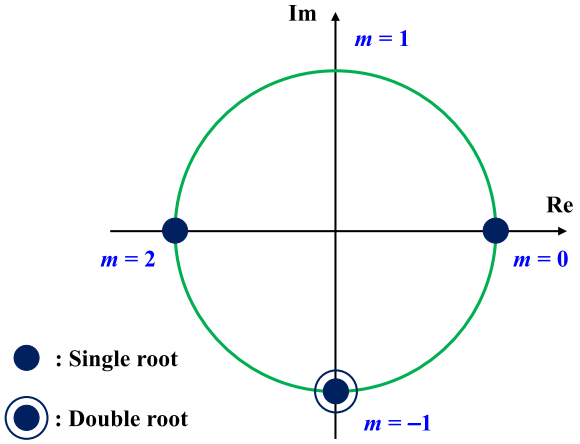

Fig. 8 Characteristic diagram of Schwider and Hariharan 5-sample algorithm [80, 81]

and 15-, 17-, and 19-sample algorithms [143–145]. The procedures for deriving the algorithms using the characteristic polynomial are discussed using the Surrel 2 $N-1$ [87] and the Kim 3 $N-2$ [98] algorithms.

Surrel located the double roots on all divided points of the characteristic diagram, except at $m=1$, to compensate for the $(N-2)$ th-order harmonics and coupling error between harmonics and the linear phase-shift error. The characteristic polynomial of this algorithm is defined as follows:

$$P_{2N-1}(x) = \left(x-\zeta^{-1}\right)^2\left(x-\zeta^{0}\right)^2\left(x-\zeta^{2}\right)^2\cdots\left(x-\zeta^{N-2}\right)^2 \tag{60}$$

Using Eqs. (45) and (46), Eq. (61) can be written using the triangular window function $[w_r]_{2N-1}$ as follows [87]:

$$P_{2N-1}(x) = \sum_{r=1}^{M}[w_r]_{2N-1}\exp\left[-i\frac{2\pi}{N}(r-N)\right]x^{r-1} \tag{61}$$

$$[w_r]_{2N-1} = N-|N-r|,\ (1\le r\le 2N-1) \tag{62}$$

To suppress the coupling error between the harmonics and first-order nonlinear phase-shift error, Kim located the triple roots on all divided points of the characteristic diagram, except at $m=1$. The characteristic polynomial of this algorithm is defined as follows:

$$P_{3N-2}(x) = \sum_{r=1}^{M}[w_r]_{3N-2}\exp\left[-i\frac{2\pi}{N}\left(r-\frac{3N-1}{2}\right)\right]x^{r-1} \tag{63}$$

where the window function of the 3 $N-2$ algorithm $[w_r]_{3N-2}$ is given to [98]

(i) $1\le r\le N$

$$[w_r]_{3N-2} = \frac{1}{2}r(r+1) \tag{64}$$

(ii) $N+1\le r\le 2N-2$

$$[w_r]_{3N-2} = \frac{1}{2}N(N+1)+(r-N)(2N-r-1) \tag{65}$$

(iii) $2N-1\le r\le 3N-2$

$$[w_r]_{3N-2} = \frac{1}{2}(3N-r-1)(3N-r) \tag{66}$$

Figure 9 shows the characteristic diagrams of the 2 $N-1$ and 3 $N-2$ algorithms for $N=8$ using Eqs. (60) and (63), respectively. From Fig. 9, it is confirmed that the 2 $N-1$ and 3 $N-2$ algorithms have double and triple roots on the characteristic diagram, respectively.

To compensate for the DC error in the calculated phase, Kim proposed the noble roots positioning method in the characteristic polynomial [107, 146, 147]. The noble roots positioning method to eliminate DC error is described.

Using Eqs. (44) and (45), the DC error caused by the first-order nonlinear phase-shift error is expressed as

$$Y_1 = -\frac{2}{N^2}\sum_{r=1}^{M}(r-\tau)^2 w_r \tag{67}$$

where τ is given by $\tau=(M+1)/2$. Because the amplitudes of conventional window functions are generally positive [137], it is necessary to develop a new window function containing negative values to compensate for the DC error.

Applying the Hermitian form to the characteristic polynomial defined in Eq. (58), the characteristic polynomial is given by

$$P(x) = \sum_{r=1}^{M}\left(G_r - iH_r\right)x^{r-\tau} \tag{68}$$

When the derivative operator D is defined as $D=x\cdot d/dx$, the second derivative of Eq. (68) is expressed as

$$D^2P(x) = \sum_{r=1}^{M}(r-\tau)^2\left(G_r - iH_r\right)x^{r-\tau} \tag{69}$$

Substituting the fundamental order of the harmonics $\zeta=\exp(2\pi i/N)$ into x of the above polynomial and using Eqs. (44) and (45), Eq. (69) can be expressed as

$$D^2P(\zeta) = \sum_{r=1}^{M}(r-\tau)^2 w_r = -\frac{Y_1N^2}{2} \tag{70}$$

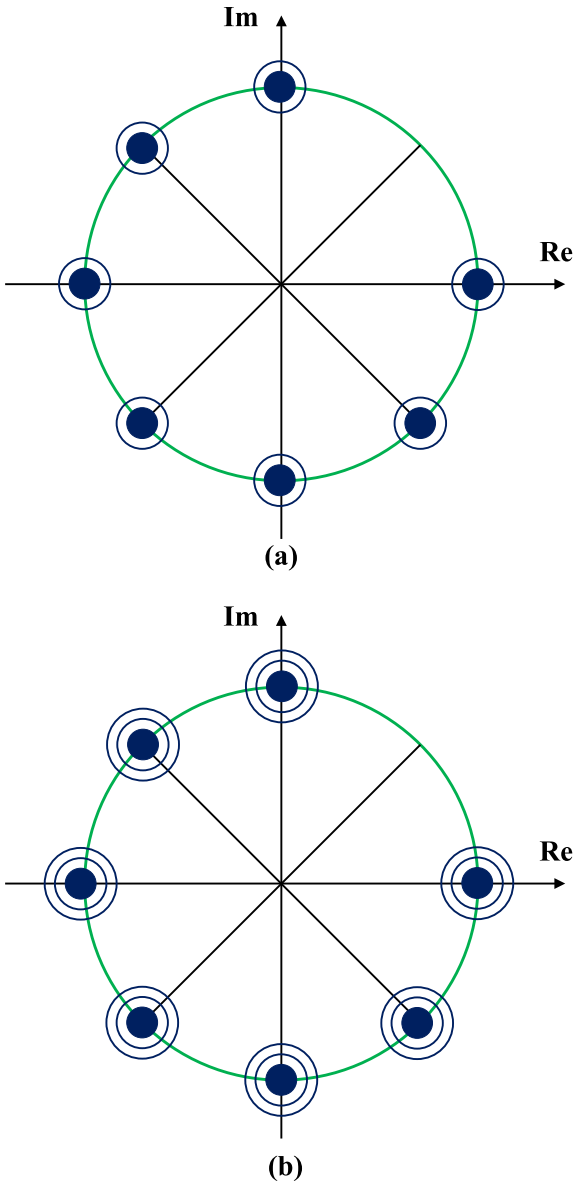

Fig. 9 Characteristic diagrams of **a** the 2 $N-1$ algorithm [87] and **b** the 3 $N-2$ algorithm [98] for $N=8$

From Eq. (70), the second-order derivative of the characteristic polynomial should have a zero value at the fundamental order of the harmonics to suppress the DC error.

A new characteristic polynomial $Q(x)$ is given to derive the phase-shifting algorithm with the suppression of the DC error as follows:

$$Q(x) = P(x) \cdot \frac{1}{x}(x - g\zeta)(x - h\zeta) \tag{71}$$

where g and h are positive values, and $1/x$ is used for the Hermitian form of $Q(x)$. Because the root should not be located in the fundamental order of the harmonics of the characteristic diagram, the positive values of g and h should not become 1. By assuming $gh=1$, Eq. (71) is given as

$$Q(x) = P(x) \cdot \left(x - \Gamma\zeta + \frac{\zeta^2}{x}\right) \tag{72}$$

where $\Gamma = g + h$.

To suppress the DC error, the second-order derivative of $Q(x)$ should have a zero value at $x=\zeta$:

$$D^2Q(\zeta) = 2\zeta \cdot P(\zeta) + \zeta(2-\Gamma) \cdot D^2P(\zeta) = 0 \tag{73}$$

Therefore, Γ can be expressed as

$$\Gamma = \frac{2P(\zeta)}{D^2P(\zeta)} + 2 \tag{74}$$

From the new root positioning method for the characteristic polynomial defined in Eqs. (72)–(74), Kim developed the 4 $N-1$ [107] and 5 $N-2$ algorithms [146], and Seo developed the 6 $N-3$ algorithm [147]. The derivation of the algorithms that can compensate for the DC error is explained using the 4 $N-1$ algorithm.

The 4 $N-1$ algorithm is derived from the 4 $N-3$ algorithm [107, 139]. The characteristic polynomial of the 4 $N-3$ algorithm is given by:

$$P_{4N-3}(x) = \sum_{r=1}^{M} [w_r]_{4N-3} \exp\left(-i\alpha_{0r}\right) x^{r-\tau}, \tag{75}$$

where the window function of the 4 $N-3$ algorithm $[w_r]_{4N-3}$ is given to [139]

(i) $1 \le r \le N$

$$[w_r]_{4N-3} = \frac{1}{6}r(r+1)(r+2) \tag{76}$$

(ii) $N+1 \le r \le 3N-3$

$$[w_r]_{4N-3} = \frac{1}{3}N\left(2N^2+1\right) + \frac{1}{2}|\Lambda|\left(|\Lambda|^2 - 2N|\Lambda| - 1\right) \tag{77}$$

where $\Lambda = r - 2N + 1$.

(iii) $3N-2 \le r \le 4N-3$

$$[w_r]_{4N-3} = \frac{1}{2}(4N-r)(4N-r-1)(4N-r-2) \tag{78}$$

Using Eqs. (76)–(78), Γ of the 4 $N-1$ algorithm is calculated as

$$\Gamma_{4N-1} = \frac{2P_{4N-3}(\zeta)}{D^2 P_{4N-3}(\zeta)} + 2 = \frac{6}{N^2-1} + 2 \tag{79}$$

Therefore, the characteristic polynomial of the 4 N – 1 algorithm can be defined using $P_{4N-3}(x)$ and Γ_{4N-1}:

$$Q_{4N-1}(x) = P_{4N-3}(x) \cdot \left[x - \left(\frac{6}{N^2-1} + 2 \right) \zeta + \frac{\zeta^2}{x} \right] \tag{80}$$

By expanding $Q_{4N-1}(x)$ and aligning the coefficients, the sampling weights of the 4 N – 1 algorithm are expressed using DFT terms and the window function of the 4 N – 1 algorithm:

$$\begin{aligned} G_r &= [w_r]_{4N-1} \cos\left[\frac{2\pi m}{N} (r - 2N) \right] \\ H_r &= [w_r]_{4N-1} \sin\left[\frac{2\pi m}{N} (r - 2N) \right] \end{aligned} \tag{81}$$

where the window function of the 4 N – 1 algorithm $[w_r]_{4N-1}$ is given to [107]

(i) $1 \le r \le N$

$$[w_r]_{4N-1} = r(r-N)(r+N) \tag{82}$$

(ii) $N+1 \le r \le 2N$

$$[w_r]_{4N-1} = -3r(r-N)(r-3N) \tag{83}$$

(iii) $3N+1 \le r \le 3N-1$

$$[w_r]_{4N-1} = 3(r-N)(r-3N)(r-4N) \tag{84}$$

(iv) $3N \le r \le 4N-1$

$$[w_r]_{4N-1} = -(r-3N)(r-4N)(r-5N) \tag{85}$$

The window functions of the 4 N – 3 and 4 N – 1 algorithms for N=8 are depicted in Fig. 10. In contrast to the 4 N – 3, the 4 N – 1 algorithm has negative values in the window function, as shown in Fig. 10b. Figure 11 shows the characteristic diagram of the 4 N – 1 algorithm for N=8. From Fig. 11, the additional roots of polynomials $g\zeta$ and $h\zeta$ defined in Eq. (70) are located on the line of the fundamental order of the harmonics.

The 4 N – 3 [139] and 4 N – 1 algorithms [107] were visualized in the frequency domain using Eqs. (13) and (14) to evaluate the phase-shifting algorithms designed by the characteristic polynomial, as discussed in Sect. 5.2. Figure 11 depicts the sampling functions of the 4 N – 3 [139] and 4 N – 1 algorithms [107].

From Fig. 12, both algorithms can compensate for the coupling error between the harmonics and second-order nonlinear phase-shift error because the third-order

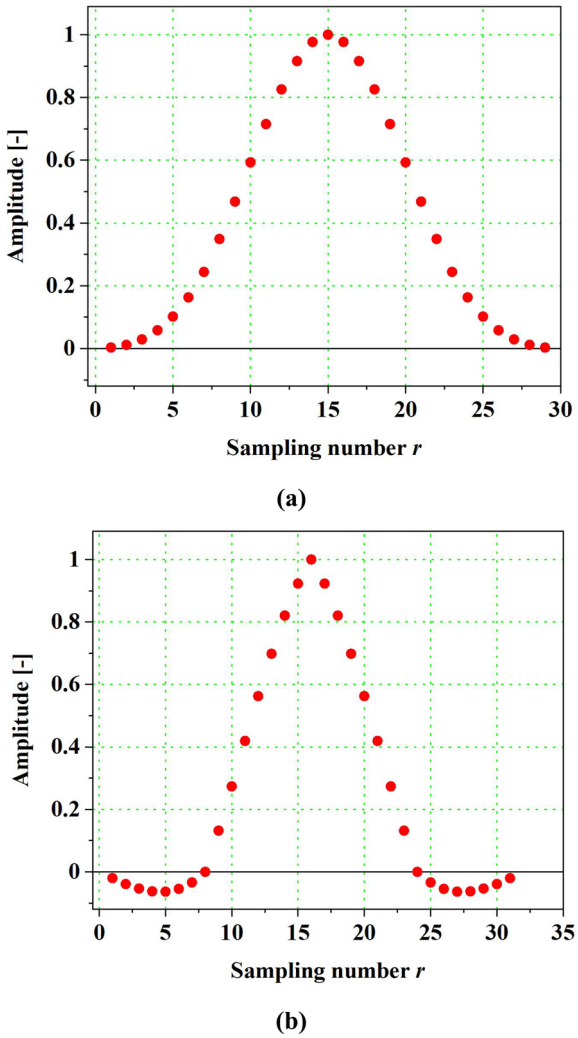

Fig. 10 Window functions of **a** the 4 N – 3 algorithm [139] and **b** the 4 N – 1 algorithm [107] for N=8

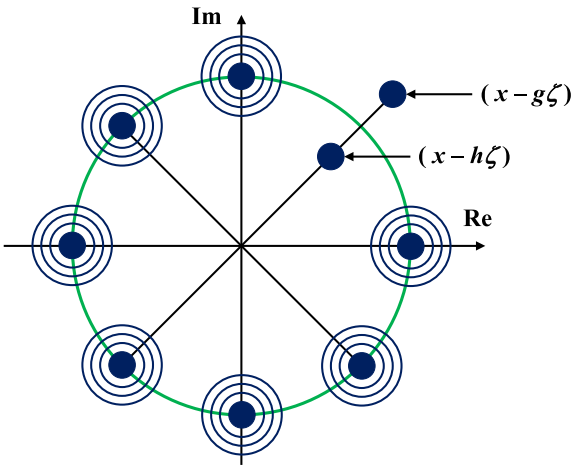

Fig. 11 Characteristic diagram of the 4 N – 1 algorithm for N=8 [107]

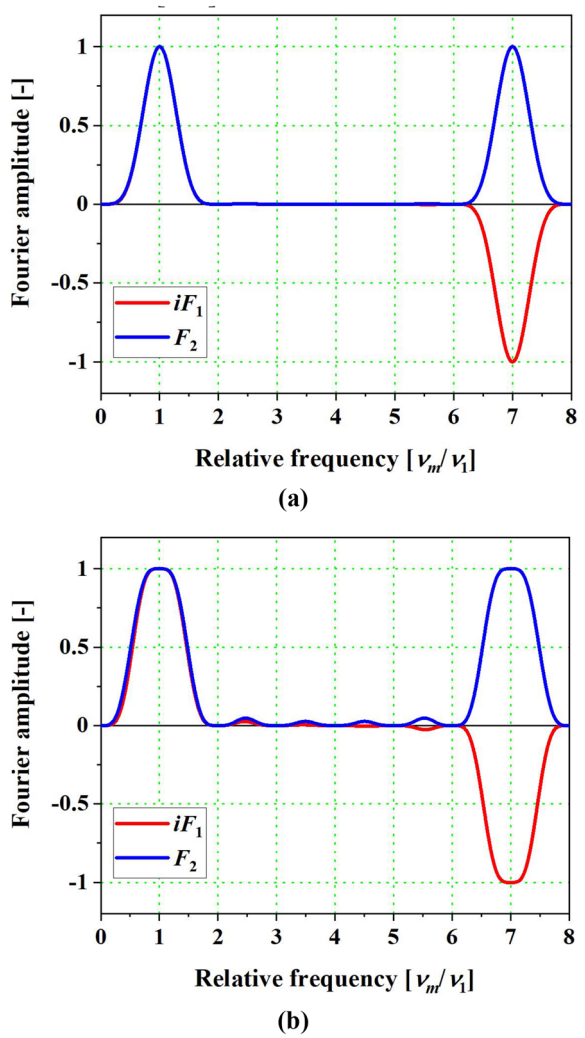

Fig. 12 Sampling functions iF_1 and F_2 of **a** 4 N – 3 algorithm [139] **b** 4 N – 1 algorithm [107]

derivatives of the sampling functions at the harmonic frequencies have a zero value. In addition, Fig. 12b shows that the 4 N – 1 algorithm has a flat configuration at the fundamental frequency, indicating that the 4 N – 1 algorithm has the suppression ability of the DC error [104].

For performance assessment of the algorithms, Surrel visualized the roots of the characteristic polynomial on a characteristic diagram [87], and Hanayama measured the glass plate surface using a Fizeau interferometer [90]. Moreover, Kim tested the glass plate and silicon wafer using a Fizeau interferometer [98, 139–145], and Seo profiled the glass plate surface and thickness using a Fizeau interferometer [147].

6 Error Compensation Ability of Phase-Shifting Algorithm

This section introduces the evaluation method of the phase-shifting algorithm in terms of the error compensation ability for the phase error.

6.1 Visibility Maximum Analysis

In the interferometric measurement of the sample surface using the phase-shifting technique, it is necessary to maximize the visibility of the interferogram [98]. Although the phase-shift error affects the visibility, eliminating the phase-shift error does not guarantee the visibility maximum. Using the sampling weights of the phase-shifting algorithm, Kim proposed the condition of the visibility maximum [98].

Equation (3) can be rewritten as follows, considering the visibility of the interferogram:

$$I(\alpha_r) = S_0 + S_1 \cos(\alpha_r + \varphi_1) = S_0[1 + V \cos(\alpha_r + \varphi_1)] \tag{86}$$

where V is the visibility of the interferogram, which can be defined by the reflectance of the reference and sample surfaces [133]. Furthermore, visibility can be defined using the sampling weights and intensity of the interferogram as follows:

$$V = \frac{1}{A}\sqrt{\left[\sum_{r=1}^{M} G_r I(\alpha_r)\right]^2 + \left[\sum_{r=1}^{M} H_r I(\alpha_r)\right]^2} \tag{87}$$

where

$$A = \frac{1}{M}\sum_{r=1}^{M} I(\alpha_r) \tag{88}$$

To derive the condition of the visibility maximum, it is assumed that phase-shift error only consists of the linear phase-shift error ε_0. By using logarithmic values and small variations for the linear phase-shift error, the visibility can be expressed as

$$\frac{\delta V}{V} = -\frac{\delta A}{A} + \frac{\delta\left\{\left[\sum_{r=1}^{M} G_r I(\alpha_r)\right]^2 + \left[\sum_{r=1}^{M} H_r I(\alpha_r)\right]^2\right\}}{2\sqrt{\left[\sum_{r=1}^{M} G_r I(\alpha_r)\right]^2 + \left[\sum_{r=1}^{M} H_r I(\alpha_r)\right]^2}} \tag{89}$$

In the equation above, δ() indicates a small variation. In Eq. (89), the first term on the right-hand side can be

neglected because of the relationship between the coefficient A and the intensity $I(\alpha_r)$ [98]. Under the assumption that the visibility maximum can be achieved at $\varepsilon_0 = 0$, the visibility should satisfy the following equation:

$$\left.\frac{dV}{d\varepsilon_0}\right|_{\varepsilon_0=0} = 0 \tag{90}$$

Substituting Eq. (89) into Eq. (90) and using Eqs. (22) and (23), the condition of the visibility maximum can be defined as:

$$\sum_{r=1}^{M} \alpha_{0r} G_r \sin \alpha_{0r} = 0 \tag{91}$$

$$\sum_{r=1}^{M} \alpha_{0r} H_r \cos \alpha_{0r} = 0 \tag{92}$$

Thus, the condition of the visibility maximum can be derived using the sampling weights of the phase-shifting algorithm.

Moreover, Kim visualized the condition of the visibility maximum using the sampling functions defined in Eqs. (13) and (14) [98]. By substituting the fundamental frequency $\nu = 1$ into the first-order derivatives of the sampling function, the following equations can be obtained:

$$\left.\frac{diF_1(\nu)}{d\nu}\right|_{\nu=1} = \sum_{r=1}^{M} \alpha_{0r} H_r \cos \alpha_{0r} \tag{93}$$

$$\left.\frac{dF_2(\nu)}{d\nu}\right|_{\nu=1} = -\sum_{r=1}^{M} \alpha_{0r} G_r \sin \alpha_{0r} \tag{94}$$

From Eqs. (91)–(94), it is evident that the phase-shift algorithm satisfies the condition of the visibility maximum when the gradients of the sampling functions at the fundamental frequency are zero. From this relationship, the condition of the visibility maximum can be visualized in the frequency domain.

The condition of the visibility maximum is discussed using the Hibino 19-sample algorithm and the Jeon 11-sample algorithm. As shown in Fig. 13, both algorithms are insensitive to the linear phase-shift error because the first derivatives of the sampling functions at the fundamental frequency are identical. However, only the 11-sample algorithm satisfies the condition of the visibility maximum because the gradients of the sampling functions are zero. It is demonstrated that the algorithm that can compensate for the linear phase-shift error may not satisfy the condition of the visibility maximum.

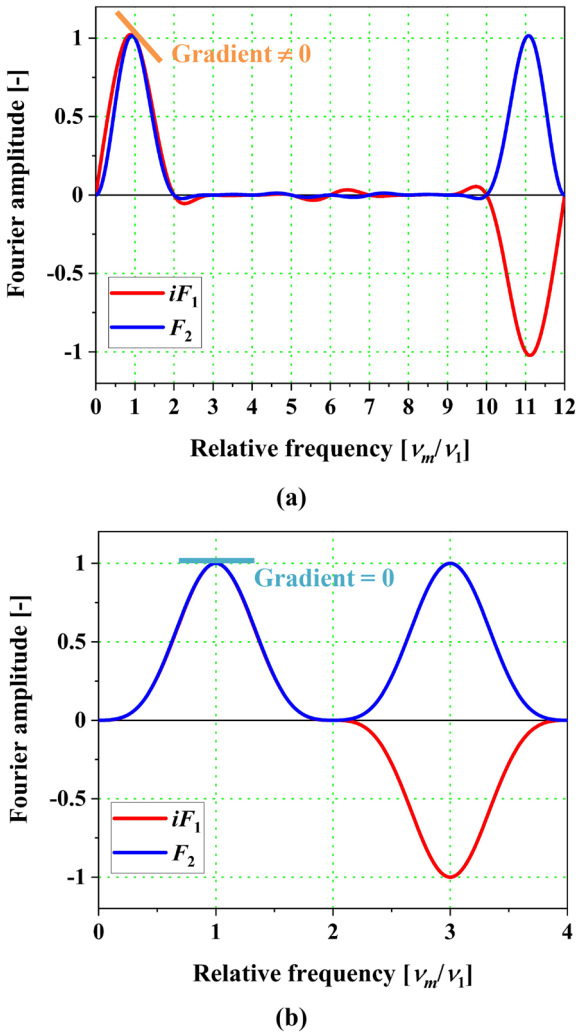

Fig. 13 Example of a gradient of the sampling functions at the fundamental frequency. **a** and **b** are the sampling functions of the Hibino 19-sample algorithm [88] and the Jeon 11-sample algorithm [92], respectively

6.2 RMS Error Analysis

De Groot and Hibino analyzed the influence of the coupling errors between harmonics and linear phase-shift errors [93, 126]. To visualize the influence of coupling errors, de Groot proposed the root mean square (RMS) phase error caused by linear phase-shift and coupling errors [126].

The RMS phase error resulting from the linear phase-shift error is expressed as

$$\sigma_{\text{lin}} = \frac{1}{2\sqrt{2}} \left| \frac{iF_1(\nu)}{F_2(\nu)} - 1 \right| \tag{95}$$

where sampling functions F_1 and F_2 are defined in Eqs. (13) and (14), respectively. The RMS phase error resulting from the coupling error between the linear phase-shift error and mth-order harmonics is given by

$$\sigma_{\text{cou}} = \frac{1}{2}\sum_{m=2}^{\infty}\frac{V_m}{V_1}\sqrt{\left[\frac{F_1(mv)}{F_1(v)}\right]^2+\left[\frac{F_2(mv)}{F_2(v)}\right]^2} \tag{96}$$

where V_m is the visibility of the mth-order harmonics [133]. Using Eqs. (95) and (96), the net RMS error is defined as

$$\sigma = \sqrt{\sigma_{\text{lin}}^2+\sigma_{\text{cou}}^2} \tag{97}$$

Figure 14 represents the solutions of the net RMS error of the phase-shifting algorithms explained in Sect. 5. As shown in Fig. 14, the RMS error is a function of the linear phase-shift error.

As shown in Fig. 14, the RMS error of the de Groot 7-sample algorithm is smaller than those of the other algorithms, implying that the de Groot 7-sample algorithm has better compensation abilities for the coupling error compared with other algorithms. Thus, the error compensation ability of the phase-shift and coupling errors can be estimated using the RMS phase error.

6.3 DC and Nonuniform Errors Analysis

Kim proposed a numerical error analysis to estimate the influence of the DC and nonuniform errors resulting from phase-shift errors [104, 107, 146]. The phase error was evaluated by numerical error analysis, considering the linear and nonlinear phase-shift errors as a function of the target phase φ_1.

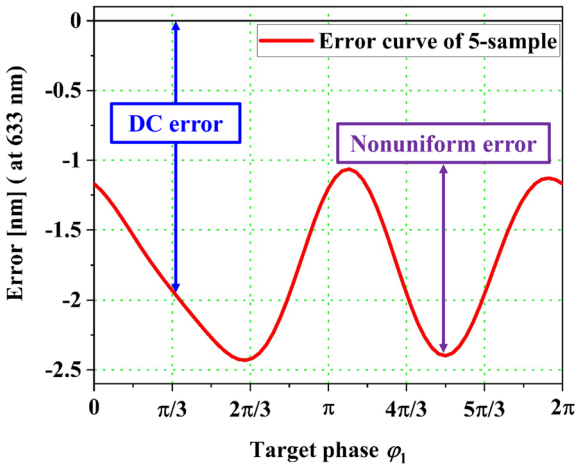

Fig. 15 DC and nonuniform errors of the Schwider and Hariharan 5-sample algorithm [80, 81]

Figure 15 shows the error curve of the Schwider and Hariharan 5-sample algorithm [80, 81] at a wavelength of 633 nm when the linear phase-shift error ε_0 is 5%, and the nonlinear phase-shift error ε_1 is 3%. In Fig. 15, the DC error is expressed as the distance between $y=0$ and the error curve. In contrast, the amplitude of the error curve corresponds to a nonuniform error.

Figure 16 shows the DC and nonuniform errors of the phase-shifting algorithms when $\varepsilon_0 = 0.05$ (5%) and $\varepsilon_1 = 0.03$ (3%). The Schwider and Hariharan 5-sample

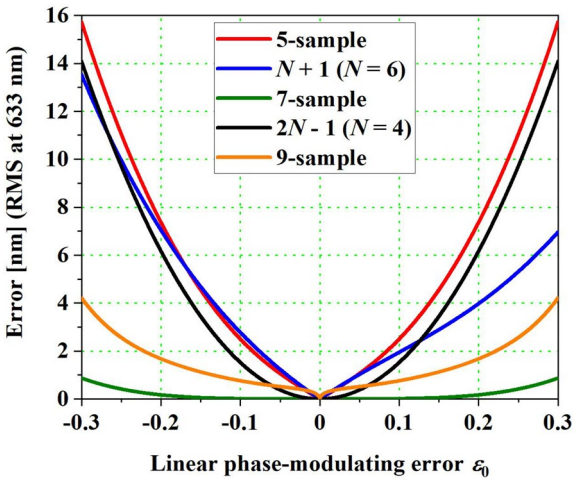

Fig. 14 RMS phase error of the phase-shifting algorithms: Schwider and Hariharan 5-sample algorithm [80, 81], Larkin and Oreb $N+1$ algorithm ($N=6$) [82], de Groot 7-sample algorithm [85], Surrel 2 N – 1 algorithm ($N=4$) [87], and Kim 9-sample algorithm [102]

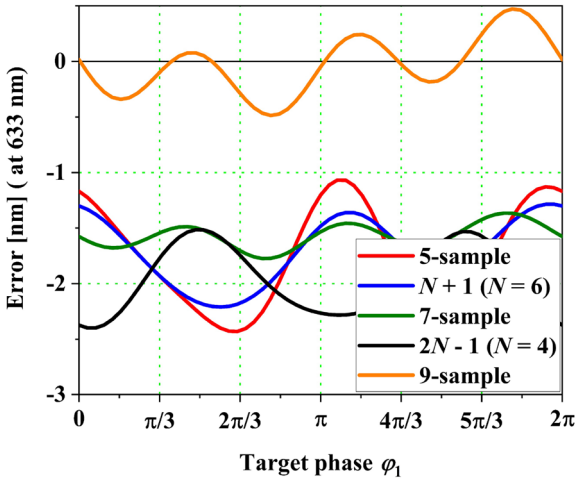

Fig. 16 DC and nonuniform errors of phase-shifting algorithms: Schwider and Hariharan 5-sample algorithm [80, 81], Larkin and Oreb $N+1$ algorithm ($N=6$) [82], de Groot 7-sample algorithm [85], Surrel 2 N – 1 algorithm ($N=4$) [87], and Kim 9-sample algorithm [102]

algorithms [80, 81] have large DC and nonuniform errors. The de Groot 7-sample algorithm [85] has a small nonuniform error but exhibits a substantial DC error of approximately 1.5 nm. In contrast, the Kim 9-sample algorithm [102] has the smallest DC error compared with the other algorithms. Therefore, using the numerical error analysis for the phase error, the compensation ability of the algorithm for the DC and nonuniform errors can be visualized.

The imperfection of optical components and mechanical parts of interferometer can be the more important factors when applying the interferometric measurement system to the industry. However, when using the commercial Fizeau interferometer (ZYGO and Fuji Film), the performances of the phase-shifting algorithms can be observed.

7 Conclusions

AS the importance of the semiconductor industry is on the rise, the surface shape and optical thickness of wafers and glass plates should be managed with nanometer measurement accuracy. To satisfy this accuracy, phase-shifting interferometry has been applied to surface and thickness measurements of wafers and glass plates. In phase-shifting interferometry, the measurement results are influenced by the performance of phase-shifting algorithms.

In this review, we discuss the design methods and performance assessment of phase-shifting algorithms in Fizeau interferometers. First, the optical setup of the Fizeau interferometer with a phase-shifting technique used for surface and thickness measurements is explained. Subsequently, the phase extraction theory and phase errors occurring in phase-shifting interferometry are described. Moreover, the design methods of the phase-shifting algorithms for the suppression of phase errors are explained, and examples of the derivation process are introduced. In addition, we discuss the evaluation methods of the error compensation abilities of the designed algorithms and present examples of the evaluation methods using several phase-shifting algorithms. Finally, we categorized the designed phase-shifting algorithms in terms of their error compensation abilities for phase errors.

Acknowledgements This study was supported by the National Research Foundation of Korea (NRF) grant funded by the Korean government (MSIT) (2021R1A2C1012658).

Data availability Due to the nature of the research, supporting data is not available.

Declarations

Conflict of interest The authors declare that they have no known competing financial interests of personal relationships that could have appeared to influence the work reported in this paper.

References

1. Rabin, O., Herz, P. R., Lin, Y. M., Akinwande, A. I., Cronin, S. B., & Dresselhaus, M. S. (2003). Formation of thick porous anodic alumina films and nanowire arrays on silicon wafers and glass. *Advanced Functional Materials, 13*(8), 631–638.
2. Kim, S.-S., & Chung, M.-K. (2021). Rapid 3D shape measurement using sine pattern in phase-shifting projection method. *International Journal of Precision Engineering and Manufacturing*, *22*(8), 1381–1389.
3. Lee, H., Kim, H., & Jeong, H. (2022). Approaches to sustainability in chemical mechanical polishing (CMP): a review. *International Journal of Precision Engineering and Manufacturing-Green Technology*, *9*(1), 349–367.
4. Ren, Z., Fang, F., Yan, N., &Wu, Y. (2022). State of the Art in Defect Detection Based on Machine Vision. *International Journal of Precision Engineering and Manufacturing-Green Technology*, *9*(2), 661–691.
5. Schmitt, R., & Doerner, D. (2006). Measurement technology for the machine-integrated determination of form deviations in optical surfaces. *CIRP Annals - Manufacturing Technology, 55*(1), 559–562.
6. Jin, J., Kim, J. W., Kim, J. A., & Eom, T. B. (2010). Thickness and refractive index measurement of a wafer based on the optical comb. *Optics InfoBase Conference Papers, 18*(17), 18339–18346.
7. Zortman, W. A., Trotter, D. C., & Watts, M. R. (2010). Silicon photonics manufacturing. *Optics Express, 18*(23), 23598–23607.
8. Fang, F. Z., Zhang, X. D., Weckenmann, A., Zhang, G. X., & Evans, C. (2013). Manufacturing and measurement of freeform optics. *CIRP Annals - Manufacturing Technology, 62*(2), 823–846.
9. Kim, J.-A., Kang, C.-S., Eom, T. B., Jin, J., Suh, H. S., & Kim, J. W. (2014). Quadrature laser interferometer for in-line thickness measurement of glass panels using a current modulation technique. *Applied Optics, 53*(20), 4604–4610.
10. de Groot, P. (2015). Principles of interference microscopy for themeasurement of surface topography. *Advances in Optics and Photonics, 7*(1), 1–65.
11. Gao, W., Kim, S. W., Bosse, H., Haitjema, H., Chen, Y. L., Lu, X. D., & Kunzmann, H. (2015). Measurement technologies for precision positioning. *CIRP Annals - Manufacturing Technology, 64*(2), 773–796.
12. Kim, D., Kim, H., Lee, S., & Jeong, H. (2015). Effect of initial deflection of diamond wire on thickness variation of sapphire wafer in multi-wire saw. *International Journal of Precision Engineering and Manufacturing - Green Technology, 2*(2), 117–121.
13. Pal, R. K., Garg, H., Sarepaka, R. G. V., & Karar, V. (2016). Experimental Investigation of Material Removal and Surface Roughness during Optical Glass Polishing. *Materials and Manufacturing Processes, 31*(12), 1613–1620.
14. Huang, Y., Ma, J., Zhu, R., Yuan, C., Chen, L., Cai, H., & Sun, W. (2015). Absolute measurement of optical flat surface shape based on the conjugate differential method. *Optics Express, 23*(23), 29687–29697.

15. Boeuf, F., Cremer, S., Temporiti, E., Fere, M., Shaw, M., Vulliet, N., Verga, L. (2015). Recent progress in silicon photonics R and D and manufacturing on 300mm wafer platform. *Optical Fiber Communication Conference, OFC 2015*, *34*(2), 286–295.
16. Lee, T., Jeong, H., Kim, H., Lee, S., & Kim, D. (2016). Effect of platen shape on evolution of total thickness variation in single-sided lapping of sapphire wafer. *International Journal of Precision Engineering and Manufacturing - Green Technology, 3*(3), 225–229.
17. Singh, A., Garg, H., Kumar, P., & Lall, A. K. (2017). Analysis and optimization of parameters in optical polishing of large diameter BK7 flat components. *Materials and Manufacturing Processes, 32*(5), 542–548.
18. Kim, J. A., Kim, J. W., Kang, C. S., Jin, J., & Lee, J. Y. (2017). An interferometric system for measuring thickness of parallel glass plates without 2π ambiguity using phase analysis of quadrature Haidinger fringes. *Review of Scientific Instruments, 88*(5), 055108.
19. Chen, B., Li, S., Deng, Z., Guo, B., & Zhao, Q. (2017). Grinding marks on ultra-precision grinding spherical and aspheric surfaces. *International Journal of Precision Engineering and Manufacturing - Green Technology, 4*(4), 419–429.
20. Pal, R. K., Sharma, R., Baghel, P. K., Garg, H., & Karar, V. (2018). An approach for quantification of friction and enhancing the process efficiency during polishing of optical glass. *Journal of Mechanical Science and Technology, 32*(8), 3835–3842.
21. Wu, M., Guo, B., Zhao, Q., Zhang, J., Fang, X., & He, P. (2019). High Efficiency Precision Grinding of Micro-structured SiC Surface Using Laser Micro-structured Coarse-Grain Diamond Grinding Wheel. *International Journal of Precision Engineering and Manufacturing - Green Technology, 6*(3), 577–586.
22. Vorburger, T. V., Rhee, H. G., Renegar, T. B., Song, J. F., & Zheng, A. (2007). Comparison of optical and stylus methods for measurement of surface texture. *International Journal of Advanced Manufacturing Technology, 33*(1–2), 110–118.
23. Shibuya, A., Gao, W., Yoshikawa, Y., Ju, B., & Kiyono, S. (2007). Profile measurements of micro-aspheric surfaces using an air-bearing stylus with a microprobe. *International Journal of precision engineering and manufacturing, 8*(2), 26–31.
24. Park, J. H., Jo, Y. K., Kim, J., & Lee, D. Y. (2012). A compact and fast nano-stylus profiling head for optical instruments. *Journal of Mechanical Science and Technology, 26*(7), 2077–2080.
25. Li, C., Yang, S., Wang, Y., Wang, C., Ren, W., & Jiang, Z. (2016). Measurement and characterization of a nano-scale multiple-step height sample using a stylus profiler. *Applied Surface Science, 387*, 732–735.
26. Tian, J., Tian, Y., Guo, Z., Wang, F., Zhang, D., Liu, X., & Shirinzadeh, B. (2016). Development of a novel 3-DOF suspension mechanism for multi-function stylus profiling systems. *International Journal of Precision Engineering and Manufacturing, 17*(11), 1415–1423.
27. Tian, J., Tian, Y., Guo, Z., Wang, F., Zhang, D., & Liu, X. (2018). Structure design and experimental investigation of a multi-function stylus profiling system for characterization of engineering surfaces at micro/nano scales. *Microsystem Technologies, 24*(5), 2177–2187.
28. Farkas, G., & Drégelyi-Kiss, K. (2018). Measurement uncertainty of surface roughness measurement. *In IOP Conference Series: Materials Science and Engineering, 448*, 012020.
29. Pawlus, P., Reizer, R., & Wieczorowski, M. (2018). Comparison of Results of Surface Texture Measurement. *Metrology and measurement systems, 25*(3), 589–602.
30. Yin, Q., Xu, B., Yin, G., Gui, P., Xu, W., & Tang, B. (2018). Surface profile measurement and error compensation of triangular microstructures employing a stylus scanning system. *Journal of Nanomaterials, 2018*, 22–24.
31. Wang, Y., Li, Z., Fu, Z., Fang, F., & Zhang, X. (2019). Radial scan form measurement for freeform surfaces with a large curvature using stylus profilometry. *Measurement Science and Technology, 30*(4), 045010.
32. Maruyama, H., Mitsuyama, T., Ohmi, M., & Haruna, M. (2000). Simultaneous measurement of refractive index and thickness by low coherence interferometry considering chromatic dispersion of index. *Optical Review, 7*(5), 468–472.
33. Murphy, D. F., & Flavin, D. A. (2000). Dispersion-insensitive measurement of thickness and group refractive index by low-coherence interferometry. *Applied Optics, 39*(25), 4607–4615.
34. Maruyama, H., Inoue, S., Mitsuyama, T., Ohmi, M., & Haruna, M. (2002). Low-coherence interferometer system for the simultaneous measurement of refractive index and thickness. *Applied Optics, 41*(7), 1315–1322.
35. Ohmi, M., Nishi, H., Konishi, Y., Yamada, Y., & Haruna, M. (2004). High-speed simultaneous measurement of refractive index and thickness of transparent plates by low-coherence interferometry and confocal optics. *Measurement Science and Technology, 15*(8), 1531–1535.
36. Kutavichus, V. P., Filippov, V. V., & Huzouski, V. H. (2006). Determination of optical parameters and thickness of weakly absorbing thin films from reflectance and transmittance spectra. *Applied Optics, 45*(19), 4547–4553.
37. Groch, D., & Poniatowska, M. (2020). Simulation tests of the accuracy of fitting two freeform surfaces. *International Journal of Precision Engineering and Manufacturing*, *21*(1), 23–30.
38. Cao, M., Zheng, P., Liu, D., Chang, J., & Zhang, L. (2021). In-process measurement and geometric error fusion control of discontinuous surface based on Bayesian theory. *International Journal of Precision Engineering and Manufacturing*, *22*(4), 539–556.
39. Onodera, R., Wakaumi, H., & Ishii, Y. (2005). Measurement technique for surface profiling in low-coherence interferometry. *Optics Communications, 254*(1–3), 52–57.
40. Sun, C., Yu, L., Sun, Y., & Yu, Q. (2005). Scanning white-light interferometer for measurement of the thickness of a transparent oil film on water. *Applied Optics, 44*(25), 5202–5205.
41. Ghim, Y.-S., & Kim, S.-W. (2006). Thin-film thickness profile and its refractive index measurements by dispersive white-light interferometry. *Optics Express, 14*(24), 11885–11891.
42. Kim, S., Na, J., Kim, M. J., & Lee, B. H. (2008). Simultaneous measurement of refractive index and thickness by combining low-coherence interferometry and confocal optics. *Optics Express, 16*(8), 5516–5526.
43. Verrier, I., Veillas, C., & Lépine, T. (2009). Low coherence interferometry for central thickness measurement of rigid and soft contact lenses. *Optics Express, 17*(11), 9157–9170.
44. Borgetto, N., André, F., Galizzi, C., & Escudié, D. (2013). Simultaneous film thickness measurement and wall temperature assessment by Low-Coherence Interferometry. *Experimental Thermal and Fluid Science, 44*, 512–519.
45. Tang, D., Gao, F., & Jiang, X. (2014). On-line surface inspection using cylindrical lens-based spectral domain low-coherence interferometry. *Applied Optics, 53*(24), 5510–5516.
46. Zhao, Y., Schmidt, G., Moore, D. T., & Ellis, J. D. (2015). Absolute thickness metrology with submicrometer accuracy using a low-coherence distance measuring interferometer. *Applied Optics, 54*(25), 7693–7700.
47. Park, H. M., & Joo, K.-N. (2017). High-speed combined NIR low-coherence interferometry for wafer metrology. *Applied Optics, 56*(31), 8592–8597.
48. Winarno, A., Takahashi, S., Matsumoto, H., & Takamasu, K. (2019). A new measurement method to simultaneously determine

group refractive index and thickness of a sample using low-coherence tandem interferometry. *Precision Engineering, 55*(2018), 254–259.
49. Chen, X., Gramaglia, M., & Yeazell, J. A. (2000). Phase-shifting interferometry with uncalibrated phase shifts. *Applied Optics, 39*(4), 585–591.
50. Cai, L. Z., Liu, Q., & Yang, X. L. (2004). Generalized phase-shifting interferometry with arbitrary unknown phase steps for diffraction objects. *Optics Letters, 29*(2), 183–185.
51. Bitou, Y., Inaba, H., Hong, F. L., Takatsuji, T., & Onae, A. (2005). Phase-shifting interferometry with equal phase steps by use of a frequency-tunable diode laser and a Fabry-Perot cavity. *Applied Optics, 44*(26), 5403–5407.
52. Yamaguchi, I., Ida, T., Yokota, M., & Yamashita, K. (2006). Surface shape measurement by phase-shifting digital holography with a wavelength shift. *Applied Optics, 45*(29), 7610–7616.
53. Xu, X. F., Cai, L. Z., Wang, Y. R., Yang, X. L., Meng, X. F., Dong, G. Y., & Zhang, H. (2007). Generalized phase-shifting interferometry with arbitrary unknown phase shifts: Direct wavefront reconstruction by blind phase shift extraction and its experimental verification. *Applied Physics Letters, 90*(12), 121124.
54. Xu, J., Jin, W., Chai, L., & Xu, Q. (2011). Phase extraction from randomly phase-shifted interferograms by combining principal component analysis and least squares method. *Optics Express, 19*(21), 20483–20492.
55. Villalobos-Mendoza, B., Granados-Agustín, F. S., Aguirre-Aguirre, D., & Cornejo-Rodríguez, A. (2015). Phase shifting interferometry using a spatial light modulator to measure optical thin films. *Applied Optics, 54*(26), 7997–8003.
56. Xu, X., Wang, Y., Ji, Y., Xu, Y., Xie, M., & Han, H. (2018). A novel dual-wavelength iterative method for generalized dual-wavelength phase-shifting interferometry with second-order harmonics. *Optics and Lasers in Engineering, 106*(January), 39–46.
57. Deck, L. L. (2003). Fourier-transform phase-shifting interferometry. *Applied Optics, 42*(13), 2354–2365.
58. Patil, A., Raphael, B., & Rastogi, P. (2004). Generalized phase-shifting interferometry by use of a direct stochastic algorithm for global search. *Optics Letters, 29*(12), 1381–1383.
59. Thakur, M., Tay, C. J., & Quan, C. (2005). Surface profiling of a transparent object by use of phase-shifting Talbot interferometry. *Applied Optics, 44*(13), 2541–2545.
60. Patil, A., & Rastogi, P. (2005). Approaches in generalized phase shifting interferometry. *Optics and Lasers in Engineering, 43*(3–5), 475–490.
61. Meng, X. F., Cai, L. Z., Xu, X. F., Yang, X. L., Shen, X. X., Dong, G. Y., & Wang, Y. R. (2006). Two-step phase-shifting interferometry and its application in image encryption. *Optics Letters, 31*(10), 1414–1416.
62. Kumar, Y. P., & Chatterjee, S. (2010). Thickness measurement of transparent glass plates using a lateral shearing cyclic path optical configuration setup and polarization phase shifting interferometry. *Applied Optics, 49*(33), 6552–6557.
63. Vargas, J., Quiroga, J. A., & Belenguer, T. (2011). Phase-shifting interferometry based on principal component analysis. *Optics Letters, 36*(8), 1326–1328.
64. Li, J., Wang, Y., Meng, X., Yang, X., & Wang, Q. (2013). An evaluation method for phase shift extraction algorithms in generalized phase-shifting interferometry. *Journal of Optics, 15*(10), 105408.
65. Deck, L. L. (2014). Model-based phase shifting interferometry. *Applied Optics, 53*(21), 4628–4636.
66. Shoji, E., Komiya, A., Okajima, J., Kubo, M., & Tsukada, T. (2019). Three-step phase-shifting imaging ellipsometry to measure nanofilm thickness profiles. *Optics and Lasers in Engineering, 112*(2018), 145–150.
67. Phillion, D. W. (1997). General methods for generating phase-shifting interferometry algorithms. *Applied Optics, 36*(31), 8098–8115.
68. Wang, Z., & Han, B. (2004). Advanced iterative algorithm for phase extraction of randomly phase-shifted interferograms. *Optics Letters, 29*(14), 1671–1673.
69. Guo, H. (2011). Blind self-calibrating algorithm for phase-shifting interferometry by use of cross-bispectrum. *Optics Express, 19*(8), 7807–7815.
70. Shi, Z., Zhang, J., Sui, Y., Peng, J., Yan, F., & Yang, H. (2011). Design of algorithms for phase shifting interferometry using self-convolution of the rectangle window. *Optics Express, 19*(15), 14671–14681.
71. Juarez-Salazar, R., Robledo-Sánchez, C., Meneses-Fabian, C., Guerrero-Sánchez, F., & Arévalo Aguilar, L. M. (2013). Generalized phase-shifting interferometry by parameter estimation with the least squares method. *Optics and Lasers in Engineering, 51*(5), 626–632.
72. Fang, C., Xiang, Y., Qi, K., Zhang, C., & Yu, C. (2013). An 11-frame phase shifting algorithm in lateral shearing interferometry. *Optics Express, 21*(23), 28325–28333.
73. Flores Muñoz, V. H., Arellano, N.-I.T., Serrano García, D. I., Martínez García, A., Rodríguez Zurita, G., & García Lechuga, L. (2016). Measurement of mean thickness of transparent samples using simultaneous phase shifting interferometry with four interferograms. *Applied Optics, 55*(15), 4047–4051.
74. Sun, T., Zheng, W., Yu, Y., Yan, K., Asundi, A., & Valukh, S. (2019). Algorithm for surfaces profiles and thickness variation measurement of a transparent plate using a Fizeau interferometer with wavelength tuning. *Applied Sciences, 9*(11), 2349.
75. Yu, J., Zhou, F., Wang, H., Xie, Y., Zhang, H., Wang, L., Jin, P., & Shui, C. (2019). Method for designing error-resistant phase-shifting algorithm. *Optics Communications, 433*, 52–59.
76. Chen, Y., Wang, T., & Kemao, Q. (2021). Parallel advanced iterative algorithm for phase extraction with unknown phase-shifts. *Optics and Lasers in Engineering, 138*, 106408.
77. Bruning, J. H., Herriott, D. R., Gallagher, J. E., Rosenfeld, D. P., White, A. D., & Brangaccio, D. J. (1974). Digital wavefront measuring interferometer for testing optical surfaces and lenses. *Applied optics, 13*(11), 2693–2703.
78. Wyant, J. C. (1975). Use of an ac heterodyne lateral shear interferometer with real–time wavefront correction systems. *Applied Optics, 14*(11), 2622–2626.
79. Wyant, J. C., Koliopoulos, C. L., Bhushan, B., & George, O. E. (1984). An optical profilometer for surface characterization of magnetic media. *ASLE transactions, 27*(2), 101–113.
80. Schwider, J., Burow, R., Elssner, K.-E., Grzanna, J., Spolaczyk, R., & Merkel, K. (1983). Digital wave-front measuring interferometry: Some systematic error sources. *Applied Optics, 22*(21), 3421–3432.
81. Hariharan, P., Oreb, B. F., & T. E. (1987). Digital phase-shifting interferometry: A simple error-compensating phase calculation algorithm. *Applied Optics, 26*(13), 2504–2506.
82. Larkin, K. G., & Oreb, B. F. (1992). Design and assessment of symmetrical phase-shifting algorithms. *Journal of the Optical Society of America A, 9*(10), 1740–1748.
83. Zhu, Y., Sugisaki, K., Ouchi, C., Hasegawa, M., Niibe, M., Suzuki, A., & Murakami, K. (2004). Lateral shearing interferometer for EUVL: theoretical analysis and experiment. In *In Emerging Lithographic Technologies VIII. SPIE* (pp. 824–832).
84. Schmit, J., & Creath, K. (1995). Extended averaging technique for derivation of error-compensating algorithms in phase-shifting interferometry. *Applied Optics, 34*(19), 3610–3619.

85. de Groot, P. (1995). Derivation of algorithms for phase-shifting interferometry using the concept of a data-sampling window. *Applied Optics, 34*(22), 4723–4730.
86. Hibino, K., Larkin, K. G., Oreb, B. F., & Farrant, D. I. (1995). Phase shifting for nonsinusoidal waveforms with phase-shift errors. *Journal of the Optical Society of America A, 12*(4), 761–768.
87. Surrel, Y. (1996). Design of algorithms for phase measurements by the use of phase stepping. *Applied Optics, 35*(1), 51–60.
88. Hibino, K., Oreb, B. F., & Fairman, P. S. (2003). Wavelength-scanning interferometry of a transparent parallel plate with refractive-index dispersion. *Applied Optics, 42*(19), 3888–3895.
89. Hibino, K., Oreb, B. F., Fairman, P. S., & Burke, J. (2004). Simultaneous measurement of surface shape and variations in optical thickness of a transparent parallel plate in wavelength-scanning Fizeau interferometer. *Applied Optics, 43*(6), 1241–1249.
90. Hanayama, R., Hibino, K., Warisawa, S., & Mitsuishi, M. (2004). Phase measurement algorithm in wavelength scanned fizeau interferometer. *Optical Review, 11*(5), 337–343.
91. Estrada, J. C., Servin, M., & J. A. Q. (2009). Easy and straightforward construction of wideband phase-shifting algorithms for interferometry. *Optics Letters, 34*(4), 413–415.
92. Jeon, J., Kim, S., & Kim, Y. (2021). Precise interferometric surface profiling of silicon wafer using sampling window and wavelength tuning. *Journal of Mechanical Science and Technology, 35*(5), 2177–2184.
93. Hibino, K., Oreb, B. F., Farrant, D. I., & Larkin, K. G. (1997). Phase-shifting algorithms for nonlinear and spatially nonuniform phase shifts. *Journal of the Optical Society of America A, 14*(4), 918–930.
94. Zhang, H., Lalor, M. J., & Burton, D. R. (1999). Robust, accurate seven-sample phase-shifting algorithm insensitive to nonlinear phase-shift error and second-harmonic distortion: A comparative study. *Optical Engineering, 38*(9), 1524–1533.
95. Zhang, H., Lalor, M. J., & Burton, D. R. (1999). Error-compensating algorithms in phase-shifting interferometry: A comparison by error analysis. *Optics and Lasers in Engineering, 31*(5), 381–400.
96. de Groot, P. (2000). Measurement of transparent plates with wavelength-tuned phase-shifting interferometry. *Applied Optics, 39*(16), 2658–2663.
97. Wu, F., Zhang, H., Lalor, M. J., & Burton, D. R. (2001). A novel design for fiber optic interferometric fringe projection phase-shifting 3-D profilometry. *Optics Communications, 187*(4–6), 347–357.
98. Kim, Y., Hibino, K., Sugita, N., & Mitsuishi, M. (2014). Design of phase shifting algorithms: Fringe contrast maximum. *Optics Express, 22*(15), 18203–18213.
99. Kumagai, T., Hibino, K., & Nagaike, Y. (2017). Dual-phase-shift spherical Fizeau interferometer for reduction of noise due to internally scattered light. *Optical Engineering, 56*(3), 034102.
100. Choque, I., Servin, M., Padilla, M., Asmad, M., & Ordones, S. (2019). Phase measurement of nonuniform phase-shifted interferograms using the frequency transfer function. *Applied Optics, 58*(15), 4157–4162.
101. Padilla, M., Servin, M., Garnica, G., & Paez, G. (2019). Design of robust phase-shifting algorithms using N-step formulas as building blocks. *Optics and Lasers in Engineering, 121*(May), 346–351.
102. Kim, Y., Hibino, K., & Mitsuishi, M. (2018). Interferometric profile measurement of optical-thickness by wavelength tuning with suppression of spatially uniform error. *Optics Express, 26*(8), 10870–10878.
103. Choque, I., Padilla, M., Servin, M., Asmad, M., & Ordones, S. (2020). Suppressing ripple distortions and spurious pistons in phase-shifting interferometry. *Journal of the Optical Society of America A, 37*(4), 614–620.
104. Kim, Y., Moon, Y., Hibino, K., & Mitsuishi, M. (2020). Thickness profiling of transparent plate using wavelength-tuned phase-shifting analysis. *Measurement, 161*, 107870.
105. Bae, W., Kim, Y., Moon, Y. H., Hibino, K., Sugita, N., & Mitsuishi, M. (2021). Simultaneous thickness variation and surface profiling of glass plates using Fizeau interferometer with elimination of offset phase error. *Optics Communications, 480*, 126500.
106. Kim, S., Kim, Y., Shin, S. C., Hibino, K., & Sugita, N. (2021). Interferometric thickness measurement of glass plate by phase-shifting analysis using wavelength scanning with elimination of bias phase error. *Optical Review, 28*(1), 48–57.
107. Kim, Y., Bae, W., Moon, Y. H., Hibino, K., & Mitsuishi, M. (2021). Fourier interferometry of multi-layer sample using wavelength tuning and partially negative window. *Optics and Lasers in Engineering, 137*, 106350.
108. Creath, K., WOLF, E. (1988) Progress in optics XXVl phase-measurement interferometry techniques.
109. Qian, K., Shu, F., & Wu, X. (2000). Determination of the best phase step of the Carre algorithm in phase shifting interferometry. *Measurement Science and Technology, 11*(8), 1220–1223.
110. Novák, J., Novák, P., & Mikš, A. (2008). Multi-step phase-shifting algorithms insensitive to linear phase shift errors. *Optics Communications, 281*(21), 5302–5309.
111. Pan, B., Kemao, Q., Huang, L., & Asundi, A. (2009). Phase error analysis and compensation for nonsinusoidal waveforms in phase-shifting digital fringe projection profilometry. *Optics Letters, 34*(4), 416–418.
112. Chen, W., Quan, C., Tay, C. J., & Fu, Y. (2009). Quantitative detection and compensation of phase-shifting error in two-step phase-shifting digital holography. *Optics Communications, 282*(14), 2800–2805.
113. de Groot, P. (2009). Design of error-compensating algorithms for sinusoidal phase shifting interferometry. *Applied Optics, 48*(35), 6788–6796.
114. Liu, F., Wu, Y., & Wu, F. (2015). Correction of phase extraction error in phase-shifting interferometry based on Lissajous figure and ellipse fitting technology. *Optics Express, 23*(8), 10794–10807.
115. Kim, Y., Hibino, K., Sugita, N., & Mitsuishi, M. (2015). Surface profile measurement of a highly reflective silicon wafer by phase-shifting interferometry. *Applied Optics, 54*(13), 4207–4213.
116. Zhai, Z., Li, Z., Zhang, Y., Dong, Z., Wang, X., & Lv, Q. (2018). An accurate phase shift extraction algorithm for phase shifting interferometry. *Optics Communications, 429*(March), 144–151.
117. Deck, L. L. (2009). Suppressing phase errors from vibration in phase-shifting interferometry. *Applied Optics, 48*(20), 3948–3960.
118. Park, J., & Kim, S.-W. (2010). Vibration-desensitized interferometer by continuous phase shifting with high-speed fringe capturing. *Optics Letters, 35*(1), 19–21.
119. Liu, Q., Wang, Y., He, J., & Ji, F. (2015). Modified three-step iterative algorithm for phase-shifting interferometry in the presence of vibration. *Applied Optics, 54*(18), 5833–5841.
120. Hao, Q., Zhu, Q., & Hu, Y. (2009). Random phase-shifting interferometry without accurately controlling or calibrating the phase shifts. *Optics Letters, 34*(8), 1288–1290.
121. Ri, S., Takimoto, T., Xia, P., Wang, Q., Tsuda, H., & Ogihara, S. (2020). Accurate phase analysis of interferometric fringes by the spatiotemporal phase-shifting method. *Journal of Optics, 22*(10), 105703.
122. Langoju, R., Patil, A., & Rastogi, P. (2007). Statistical study of generalized nonlinear phase step estimation methods in phase-shifting interferometry. *Applied Optics, 46*(33), 8007–8014.

123. Langoju, R., Patil, A., & Rastogi, P. (2007). A novel approach for characterizing the nonlinear phase steps of the PZT in interferometry. *Optics and Lasers in Engineering, 45*(2), 258–264.
124. Langoju, R., Patil, A., & Rastogi, P. (2006). Phase-shifting interferometry in the presence of nonlinear phase steps, harmonics, and noise. *Optics Letters, 31*(8), 1058–1060.
125. Kim, Y., Hibino, K., Sugita, N., & Mitsuishi, M. (2015). Absolute optical thickness measurement of transparent plate using excess fraction method and wavelength-tuning Fizeau interferometer. *Optics Express, 23*(4), 4065–4073.
126. de Groot, P. J. (2014). Correlated errors in phase-shifting laser Fizeau interferometry. *Applied Optics, 53*(19), 4334–4342.
127. Schwider, J. (1993). New compensating four-phase algorithm for phase-shift interferometry. *Optical Engineering, 32*(8), 1883–1885.
128. Zhu, R., Chen, J., Wang, Q., Chen, L., & Zhang, Y. (1993). New algorithm on phase-shifting interferometry: The overlapping averaging 4-frame algorithm. In *In: Interferometry VI: Techniques and Analysis. SPIE* (pp. 355–366).
129. Freischlad, K., & Koliopoulos, C. L. (1990). Fourier description of digital phase-measuring interferometry. *Journal of the Optical Society of America A, 7*(4), 542–551.
130. Servin, M., Estrada, J. C., & Quiroga, J. A. (2009). Spectral analysis of phase shifting algorithms. *Optics Express, 17*(19), 16423–16428.
131. Servin, M., Estrada, J. C., & Quiroga, J. A. (2009). The general theory of phase shifting algorithms. *Optics Express, 17*(24), 21867–21881.
132. Hibino, K. (1997). Susceptibility of systematic error-compensating algorithms to random noise in phase-shifting interferometry. *Applied Optics, 36*(10), 2084–2093.
133. Hibino, K. (1999). Error-compensating phase measuring algorithms in a fizeau interferometer. *Optical Review, 6*(6), 529–538.
134. Hibino, K., & Takatsuji, T. (2002). Suppression of multiple-beam interference noise in testing an optical-parallel plate by wavelength-scanning interferometry. *Optical Review, 9*(2), 60–65.
135. Hibino, K., & Yamauchi, M. (2000). Phase-measuring algorithms to suppress spatially nonuniform phase modulation in a two-beam interferometer. *Optical Review, 7*(6), 543–549.
136. Bae, W., & Kim, Y. (2021). Phase extraction formula for glass thickness measurement using Fizeau interferometer. *Journal of Mechanical Science and Technology, 35*(4), 1623–1632.
137. Harris, F. J. (1978). On the Use of Windows for Harmonic Analysis with the Discrete Fourier Transform. *Proceedings of the IEEE, 66*(1), 51–83.
138. Surrel, Y. (1993). Phase stepping: A new self-calibrating algorithm. *Applied Optics, 32*(19), 3598–3600.
139. Kim, Y., Hibino, K., Hanayama, R., Sugita, N., & Mitsuishi, M. (2014). Multiple-surface interferometry of highly reflective wafer by wavelength tuning. *Optics Express, 22*(18), 21145–21156.
140. Kim, Y., Sugita, N., & Mitsuishi, M. (2016). Measurement of highly reflective surface shape using wavelength tuning Fizeau interferometer and polynomial window function. *Precision Engineering, 45*, 187–194.
141. Kim, Y., Hibino, K., Sugita, N., & Mitsuishi, M. (2015). Simultaneous measurement of surface shape and optical thickness using wavelength tuning and a polynomial window function. *Optics Express, 23*(25), 32869–32880.
142. Kim, Y., Hibino, K., Sugita, N., & Mitsuishi, M. (2016). Interferometric measurement of surface shape by wavelength tuning suppressing random intensity error. *Applied Optics, 55*(23), 6464–6470.
143. Kim, Y., Hibino, K., Sugita, N., & Mitsuishi, M. (2015). Measurement of optical thickness variation of BK7 plate by wavelength tuning interferometry. *Optics Express, 23*(17), 22928–22938.
144. Kim, Y., & Hibino, K. (2017). Statistical and interferometric determination of the optical thickness of a multilayer transparent plate. *Optical Review, 24*(6), 734–740.
145. Kim, Y., Sugita, N., & Mitsuishi, M. (2017). Phase-measuring algorithm to suppress inner reflection of transparent parallel plate in wavelength tuning Fizeau interferometer. *Precision Engineering, 48*, 67–74.
146. Kim, Y., Seo, J., Bae, W., Moon, Y. H., Ito, Y., & Sugita, N. (2021). Wavelength-modulation Fourier interferometry with elimination of DC phase error. *Precision Engineering, 68*, 97–105.
147. Seo, J., Kim, Y., Bae, W., Moon, Y. H., & Sugita, N. (2021). Wavelength-tuning multiple-surface interferometric analysis with compression of Zernike piston phase error. *Measurement, 185*, 110078.

Publisher's Note Springer Nature remains neutral with regard to jurisdictional claims in published maps and institutional affiliations.

Springer Nature or its licensor (e.g. a society or other partner) holds exclusive rights to this article under a publishing agreement with the author(s) or other rightsholder(s); author self-archiving of the accepted manuscript version of this article is solely governed by the terms of such publishing agreement and applicable law.

Sungtae Kim received his B. S. degree at the School of Mechanical Engineering, Pusan National University in 2019. He is Ph. D. candidate at the School of Mechanical Engineering, Pusan National University. His research interests include precision measurement using wavelength-scanning Fizeau interferometer and fringe analysis using iterative algorithm.

Jurim Jeon received her B. S. degree at the School of Mechanical Engineering, Pusan National University in 2021. She is a master and doctor integrated course student at the School of Mechanical Engineering, Pusan National University. Her research interests include precision measurement using wavelength-scanning Fizeau interferometer and fringe analysis using deep learning.

Yangjin Kim received his B. S. and Ph. D. degrees at the Department of Mechanical Engineering, The University of Tokyo, in 2007 and 2015, respectively. He was a technical research personnel at the Korea Institute of Machinery and Materials (KIMM) from 2009 to 2012 as a military service. He is an Associate Professor at the School of Mechanical Engineering, Pusan National University. His research interests include precision measurement using wavelength-scanning Fizeau interferometer and fringe analysis using phase modulating. He is a member of Korean Society for Precision Engineering, The Korean Society of Mechanical Engineers, The Japan Society for Precision Engineering, The American Society of Mechanical Engineers, and The International Society for Optics and Photonics.

Naohiko Sugita received his M. S. and Ph. D. degrees at the Department of Mechanical Engineering, The University of Tokyo, in 1996 and 2005, respectively. He was with NEC, Tokyo, Japan, from 1996 to 2003. He was also a Research Associate and an Associate Professor with The University of Tokyo, in 2003 and 2007, respectively. He is a Professor at the Department of Mechanical Engineering, The University of Tokyo from 2014. His research interests include the machining of biomaterials, robot-assisted surgical systems, and intelligent manufacturing systems.

Mamoru Mitsuishi received his M. S. and D. E. degrees at the Department of Mechanical Engineering, The University of Tokyo, in 1983 and 1986, respectively. In 1986, he was a Lecturer with The University of Tokyo, where he was also an Associate Professor in 1989 and a Professor since 1999. From 1987 to 1988, he was a Visiting Researcher with the Fraunhofer Institute for Production Technique and Automation, Stuttgart, Germany. His research interests include computer integrated surgical systems and manufacturing systems. He is a member of The International Academy for Production Engineering (CIRP, Fellow, and President from 2019 to 2021), The Japan Society of Mechanical Engineers (Fellow), The Japan Society for Precision Engineering, The Robotic Society of Japan (Fellow), and IEEE Robotics and Automation Society.